arXiv:2607.02764v1 [cs.RO] 2 Jul 2026

MorphQuad: Morphable Quadrotor for Superhuman Maneuverability, Manipulation, and Resiliency

José Díaz Peón González Pacheco,* Jiawei Xu,* Andrew Zhao,* Hongyu Zhou,†
Atharva Navsalkar,† Andrew Scheffer,† Amrith Malli Reddi,† Sashreek Shankar,†
Yuqing (Ivan) Bao,† Vasileios Tzoumas

Aerospace Engineering, University of Michigan.

*Equal first-author contribution †Equal second-author contribution

Infrastructure maintenance, contact-based inspection, and emergency response can benefit from aerial vehicles that act as a flying human hand with extreme maneuverability, manipulation, and resiliency (MMR): *maneuverability* to fly in arbitrary orientations to reach remote and tight locations; *manipulation* to point sensors, turn valves, and press tools at arbitrary orientations; *resiliency* to maintain accurate motion and force control despite disturbances from arbitrary directions, such as wind, ground effects, and friction. Realizing MMR on aerial vehicles requires not only omnidirectional flight; it also requires (I) vectoring of maximum thrust in any direction, to maximize capacity for contact-force application and disturbance rejection, (II) global stability, to enable control over any orientation/position, and (III) compact, standard designs that build upon platforms such as quadrotors to inherit technological know-how. No current aerial vehicle simultaneously enables I–III, due to structural and control limitations that constrain actuation. We present MorphQuad: a morphable quadrotor that enjoys MMR. Key to our approach is a hardware and control co-design: on hardware, we inde-

pendently articulate each of the four rotor systems via two-axis gimbals; on control, we introduce globally-stable control, and energy-optimal thrust allocation that permits inter-rotor thrust cancellations only to avoid downwash interference and gimbal lock. With fully-onboard autonomy, MorphQuad demonstrates multi-revolution rotation while translating or hovering, for pipe inspection and target tracking (maneuverability); valve turning, perching, and object pressing and pushing with human-level strengths (manipulation); and wind rejection from any direction, even directed to a single rotor, and push-pull recovery (resiliency).

Summary

An autonomous morphable quadrotor that flies, perches, pulls, and turns valves in any direction under high winds and wakes.

Introduction

Infrastructure maintenance (*1, 2*), contact-based inspection (*3, 4*), and emergency response (*5–7*) can benefit from aerial vehicles that act as a flying human hand with extreme maneuverability, manipulation, and resiliency (MMR): **(a) Maneuverability**: to reach remote locations (*8, 9*), traverse tight spaces (*10–12*), and inspect complex infrastructure, such as around and in-between pipes and ducts (*13, 14*) from any direction. **(b) Manipulation**: to push obstacles away (*15*), turn valves (*16*), and press sensors against infrastructure to assess structural integrity (*4*). **(c) Resiliency**: to move and apply forces with accuracy despite challenging disturbances, such as wind (*17, 18*), wall, ceiling, and ground effects (*19, 20*), and counter-acting contact forces, *e.g.,* friction (*21, 22*).

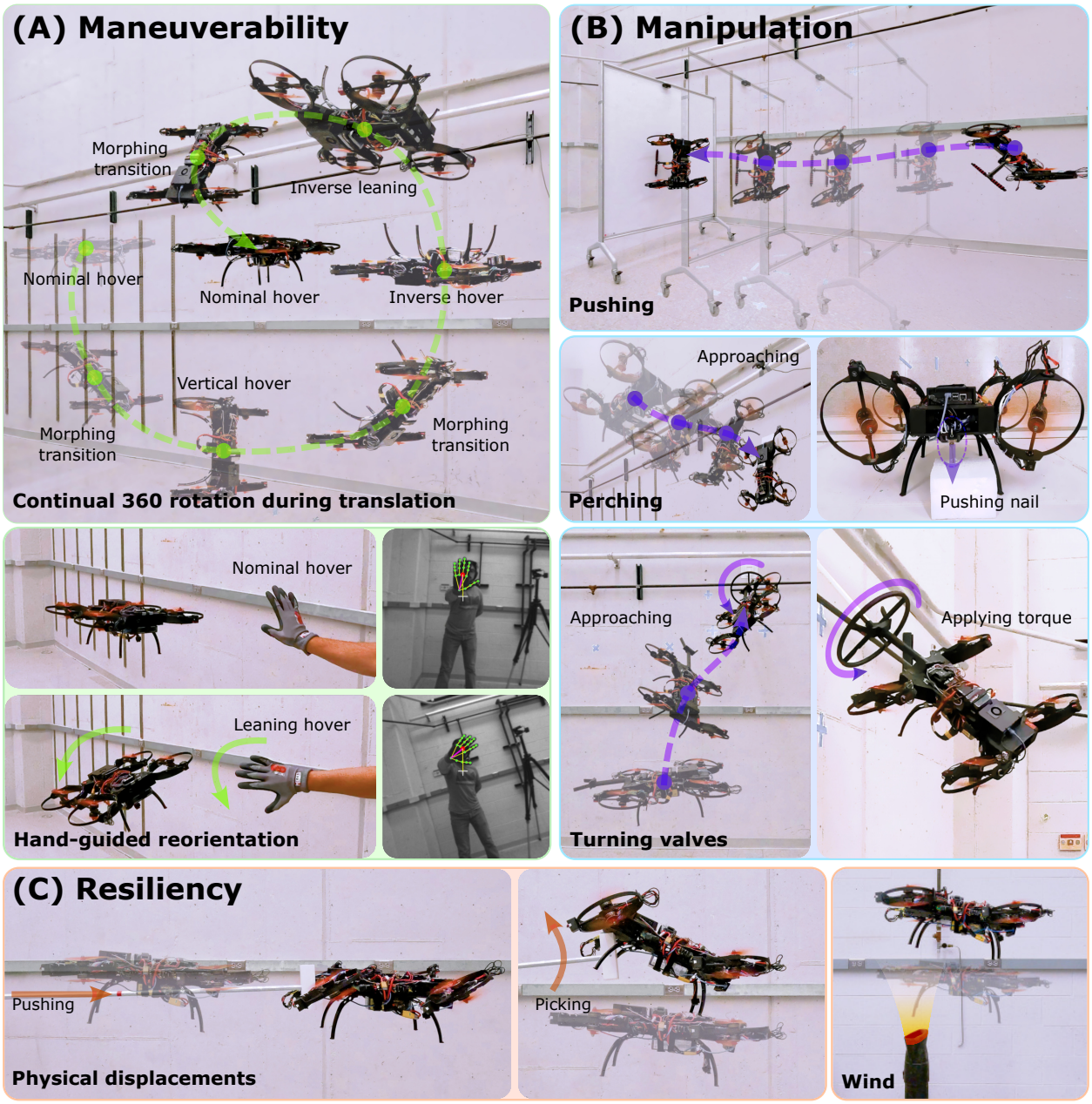

Figure 1: We present MorphQuad, a morphable quadrotor with extreme maneuverability, manipulation, and resiliency (MMR). In hardware experiments with fully-onboard autonomy (no motion capture), MorphQuad demonstrates **(A)** maneuverability, to perform multi-revolution rotation while translating around a pipe or pointing at arbitrary directions while hovering; **(B)** manipulation, for pushing heavy objects, perching on walls and pressing nails, and turning valves at arbitrary orientations; and **(C)** resiliency, for disturbance rejection under physical pushes and pulls, sustained tether forces, and strong wind from arbitrary directions.

Realizing MMR on aerial vehicles requires more than omnidirectional flight, *i.e.*, flying in arbitrary directions at any attitude; it also demands (I) vectoring of maximum thrust in any direction, (II) almost-everywhere/global stability, and (III) compact and standard designs. **Enabler I: Vectoring of maximum thrust in any direction.** Generating maximum thrust in any desired direction —up to the capacity of the vehicle's rotors and independently of vehicle orientation— delivers maximum acceleration, contact force application, and disturbance rejection along any direction. **Enabler II: Almost-everywhere/global stability.** Maintaining stability during motion from any current position and orientation to any other guarantees reliable maneuverability and manipulation amid disturbances. **Enabler III: Compact and standard designs.** Building on compact and standard platforms, such as quadrotors, the vehicle can access confined environments, inherit technological maturity, and maintain a low-complexity structure.

No current aerial vehicle enjoys simultaneously Enablers I–III: structural and control limitations either constrain the range of actuation, preventing Enablers I and/or II (*1, 16, 23–37*), or require non-compact designs of vehicle-of-vehicles (*38–40*) or hexarotor/octarotor designs (*2, 3, 41, 42*), preventing Enabler III. We next review the state of the art in more detail, from fixed-tilt to variable-tilt designs, and summarize the most relevant platforms in Table 1.

Table 1: Comparison of the most relevant omnidirectional multirotors: no current multirotor simultaneously achieves Enablers I–III. Specifically, their structural and control limitations either constrain the range of actuation, thus preventing Enablers I and/or II, or impose complex vehicle-of-vehicles and non-compact hexarotor and octarotor designs, thus preventing Enabler III.

		Enablers of maneuverability, manipulation, and resiliency			**Hardware validation**		
		Vectoring of maximum thrust in any direction	Almost-everywhere stable control	Compact and standard design	Onboard sensing and control	Manipulation on top of omnidirectional flight	Disturbance rejection
Fixed-tilt	Yang, 2018 (*1, 16, 24*)	✗	✓	✗	✗	✓	✓
	Lee, 2024 (*27*)	✗	✓	✗	✗	✗	✗
	Veenstra, 2026 (*28*)	✗	✗	✗	✗	✓	✗
Variable-tilt	Ryll, 2014 (*31, 32*)	✗	✗	✓	✗	✗	✗
	Kamel, 2018 (*34*)	✗	✗	✗	✗	✓	✗
	Ji, 2019 (*35*)	✗	✓	✗	✗	✗	✗
	Bodie, 2020 (*3, 41, 42*)	✗	✓	✗	✗	✓	✓
	Su, 2021 (*38*)	✓	✗	✗	✗	✗	✗
	Zhao, 2023 (*39, 40*)	✓	✗	✗	✗	✓	✗
	SkyGauge, 2023 (*36*)*	✗	✗	✓	✓	✓	✓
	Li, 2025 (*33*)	✗	✗	✓	✗	✗	✗
	Lee, 2025 (*2*)	✗	✓	✗	✗	✓	✓
	Aerix, 2025 (*43, 44*)*	✗	✗	unknown	✓	✗	✓
Ours	MorphEUS, 2025 (*45*)	✓	✓	✓	✗	✗	✗
	MorphQuad (this paper)	✓	✓	✓	✓	✓	✓

*No peer-reviewed publications; assessed from public patent information.

Fixed-tilt multirotors. Fixed-tilt multirotors lack Enabler I and cannot simultaneously realize Enablers II and III. Fixed-tilt multirotors lack rotor articulation: each rotor generates thrust in a static direction with respect to the vehicle body. **(a) Fixed-tilt multirotors with all rotors pointing in the same direction**, such as standard quadrotors, achieve Enabler III but not Enablers I and II. The rotors collectively generate maximum thrust only in a single direction (*46–50*), falling short of Enabler I. This also causes the inability to translate or apply force in lateral directions without rotating, falling short of Enabler II. **(b) Fixed-tilt multirotors with rotors pointing in different directions** achieve Enabler II but not Enablers I and III. Omnidirectionality on this configuration requires a large number of rotors oriented in fixed, different directions on the vehicle body (*51–54*): seven or more unidirectional rotors (*23, 25, 26*), or six or more bidirectional rotors (*1, 24, 27, 28*), all in optimized placement. Such designs impose complex mechatronic hardware and boxy structures (*23, 25, 26*), falling short of Enabler III. In addition, they always have rotors generating counteracting thrust during operation, falling short of Enabler I.

Variable-tilt multirotors. Existing variable-tilt multirotors lack Enabler I due to the limited ranges of rotor articulation (*2, 3, 30–34, 36, 41, 42, 55–58*) or thrust allocation constraints imposed by the vehicle design (*35*); those that fulfill Enabler I cannot achieve Enabler III because of their structural bulkiness (*38–40*). **(a) Variable-tilt multirotors with limited rotor articulation** sacrifice Enabler I and cannot simultaneously achieve Enablers II and III. The limited articulation, if not mechanically bounding the maximum tilting angle (*36, 37, 56*), causes inter-rotor thrust cancellation whenever the vehicle operates away from nominal hover, falling short of Enabler I. Designs in this category realize the limited articulation through either synchronized or independent single-axis rotor articulation. Synchronized rotor articulation (*30, 36, 55–58*) falls short of Enabler II due to control singularity (*30, 55*) and mechanical constraints (*36, 56*). Independent single-axis rotor articulation either empowers a quadrotor structure to achieve Enabler III but sacrifices Enabler II (*31–33*) due to control singularities, or empowers a many-rotor vehicle to achieve Enabler II (*2, 3, 34, 41, 42*) but sacrifices Enabler III, requiring complex mechatronic components that sup-

port six or more rotors in a non-compact structure. **(b) Variable-tilt multirotors with omnidirectional rotor articulation** fall short on at least one among Enablers I–III. Vehicle-of-vehicle designs, through chaining (*39, 40*) or gimbaling (*38*) smaller multirotor modules, achieve neither Enabler III, due to complex interconnection structures and mechatronics, nor Enabler II, due to the absence of stability proofs of the proposed controllers. Single-vehicle designs include the tilting quadcopter (*35*) and Aerix quadrotor (*43*): (*35*) presents a conceptual quadrotor with dual-axis rotor articulation, without specifying how this articulation is achieved via appropriate structural and hardware components. Each rotor of the tilting quadcopter is equipped with a single propeller that induces an aerodynamic drag torque when generating thrust, and a gyroscopic torque when articulating the spinning rotors; as the controller compensates these torques even during hover, the rotors spend thrust on the torque compensations, falling short of Enabler I. (*43*) is a hardware patent that presents a quadrotor structural design that enables omnidirectional rotor-tilting, but its real-world hardware implementation is not public; thus, its complexity is unknown. Further, neither control nor thrust allocation algorithms have been published or disclosed for this vehicle, nor are known to exist (*44*), obstructing Enablers I and II. We previously presented MorphEUS (*45*), a morphable quadrotor design that promises Enablers I–III through co-designed control and thrust allocation on two-axis articulated rotors; its hardware implementation, real-world deployment, and resiliency under disturbances remained open.

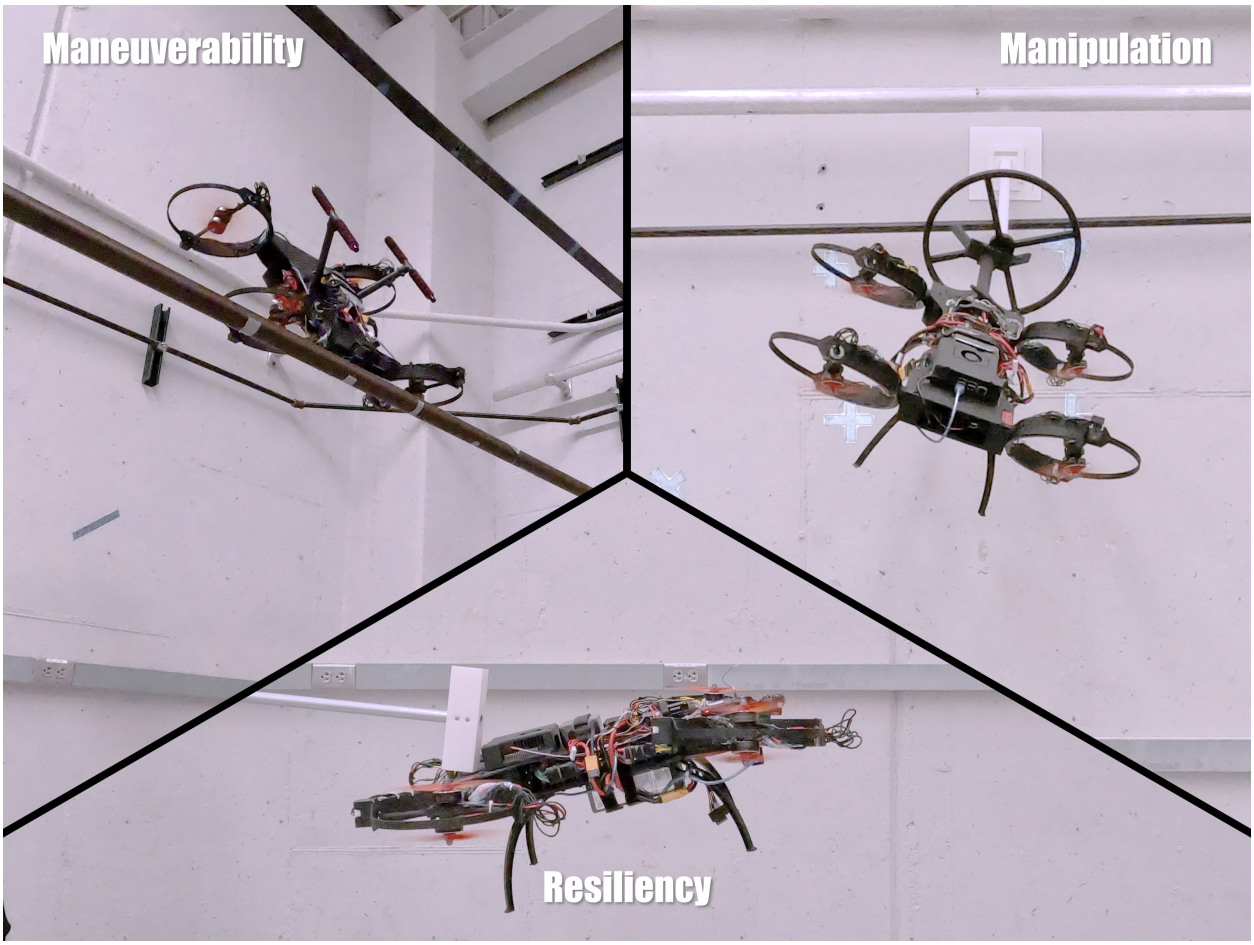

Movie 1: Overview movie of MorphQuad: We present a morphable quadrotor capable of omnidirectional free and in-contact flight —to transform infrastructure maintenance, contact-based inspection, and emergency response. The quadrotor moves like a flying human hand: it can perch, push, and pull in any direction; turn inclined valves; and perform helical multi-revolution maneuvers to inspect pipes. We demonstrate fully autonomous operation, with resilience to wind, rotor-wake, and impulsive push and pull disturbances.

Contributions

We present MorphQuad, a morphable multirotor that embodies Enablers I–III in a quadrotor structure, with fully-onboard localization and computation for (a) maneuverability, (b) manipulation, and (c) resiliency (Movie 1). **(a) Maneuverability:** MorphQuad performs helical multi-revolution motion while pointing the camera at a pipe—unprecedented on variable-tilt multirotors— for inspection, and pointing while hovering for hand tracking. **(b) Manipulation:** MorphQuad can apply torque of 4.92 Nm and lateral force of 4.55 kg, comparable to a human wrist's strength (*59*) and sufficient for industrial applications (*60*), on top of hovering. We demonstrate these in valve turning, wall perching and nail pressing, and whiteboard pushing. **(c) Resiliency:** MorphQuad maintains accurate and stable hover at any attitudes under wind disturbances —even when the wind is directed at a single rotor system.[1] Under impulsive and sustained physical displacements, MorphQuad maintains an RMSE similar to free flight on the orthogonal axes to the disturbances.

Key to our approach is a co-design of hardware and control: on hardware, we independently articulate each of the four rotor systems via two-axis gimbals for omnidirectional thrust vectoring; on control, we introduce a thrust allocation that is energy-optimal, achieving maximum thrust vectoring in any direction, and a generalized geometric controller that is almost-globally stable, which we augment with disturbance adaptation; the thrust allocation allows inter-rotor cancellation only to reduce downwash interference and avoid mechanical gimbal lock.

[1] We apply an airflow from a wind blower to the vehicle (30 m/s measured at the vehicle), producing non-uniform force and torque disturbances at a small area on the vehicle; it provides a challenge on the vehicle stability, comparable to the 10–20 m/s uniform freestream generated by a wind tunnel (*18*) or fan array (*61*).

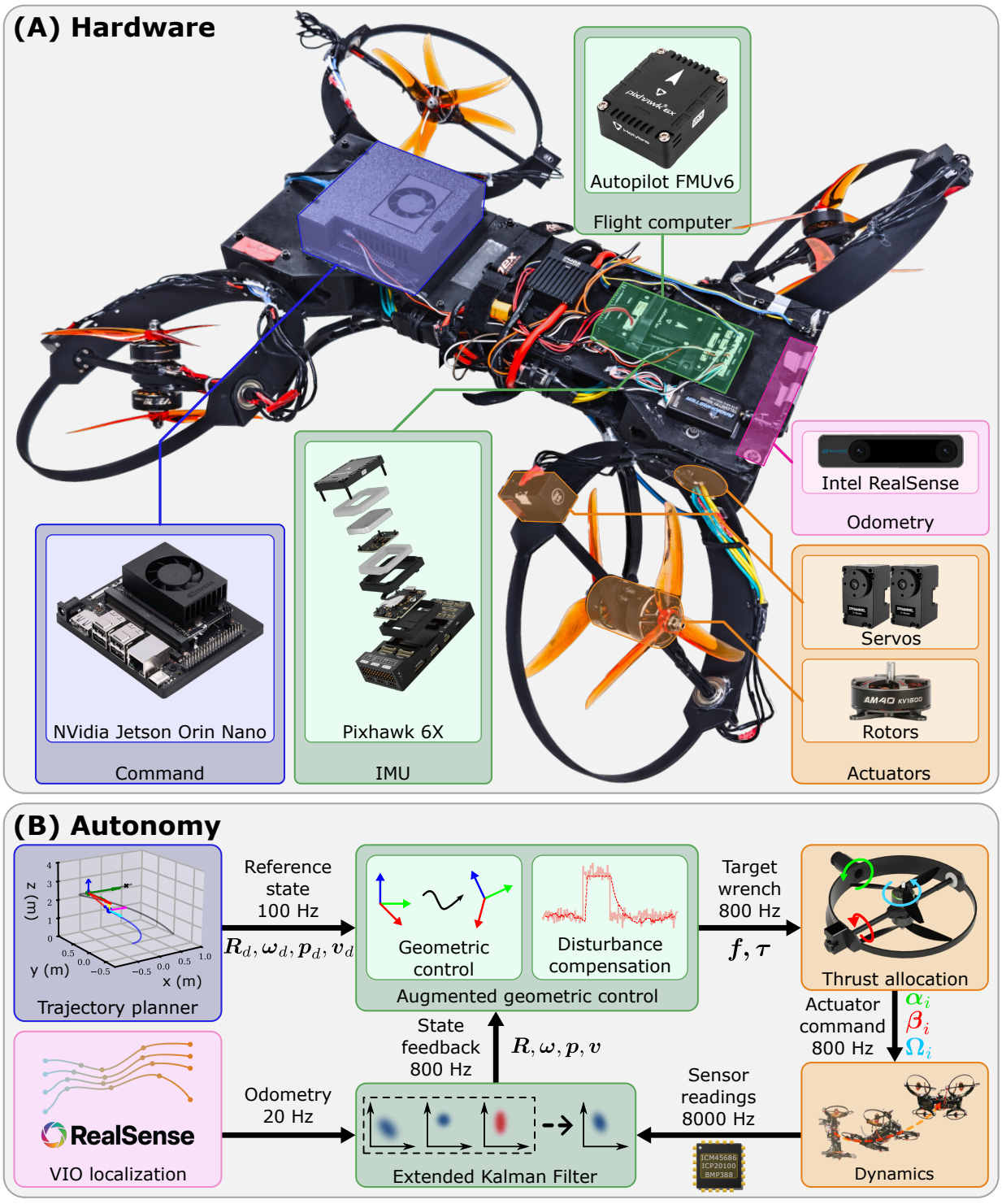

Figure 2: **(A)** Major hardware components on MorphQuad that enable omnidirectional flight. **(B)** The autonomy pipeline of MorphQuad, color-coded by its corresponding hardware in (A).

Results

First, we discuss our contributions on hardware and autonomy that embody Enablers I–III, and then showcase the hardware experiment setup and evaluation results.

Hardware and autonomy

We present MorphQuad's (A) hardware and (B) autonomy pipeline, as shown in Figure 2, co-designed to realize Enablers I–III. Replacing the regular quadrotor's fixed rotors with four independently articulated rotor systems allows MorphQuad to continuously vector maximum thrust in any direction (**Enabler I**). We deploy a provably-stable generalized geometric controller, paired with an energy-optimal thrust allocation, to guarantee almost-everywhere stability for MorphQuad (**Enabler II**). We integrate an off-the-shelf vision-based navigation architecture on a compact and standard quadrotor structure with fully-onboard autonomy (**Enabler III**).

We first present the independently articulated rotor system that enables continuous omnidirectional thrust vectoring, and then the autonomy pipeline that enables trajectory generation, localization, and motion control for the fully-onboard experiments. Additional details on mechatronic component selection and control synthesis are given in Materials and Methods.

Independently articulated rotor systems

We enable the continuous omnidirectional thrust vectoring on MorphQuad by mounting each rotor system on a gimbal mechanism (Figure 3(A)) that is actuated across two perpendicular articulation axes. The gimbals can continuously vector the rotor thrusts into any desired direction inside a sphere. Each rotor system, in particular, is composed of two counter-rotating motors with the same speed, and appropriate propellers that together generate thrust in the same direction. This design choice eliminates gyroscopic precession of the rotating motor masses and the aerodynamic drag effects from the propellers. Next, we elaborate on the gimbal design and rotor system.

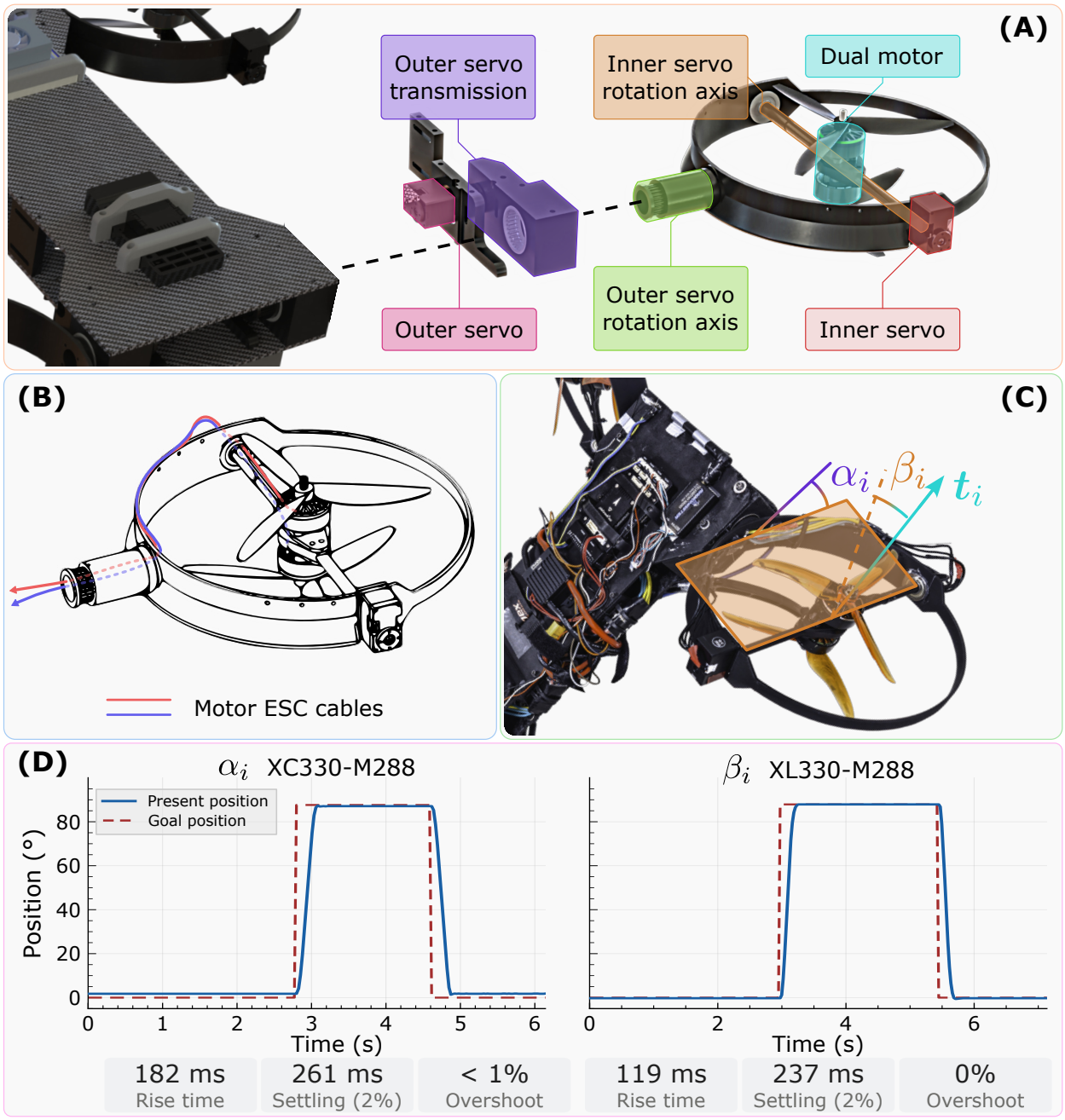

Figure 3: Each rotor system pairs two stacked motors with a two-axis gimbal, pointing the thrust in any direction while both axes spin continuously. **(A)** The inner servo rotates the motor pair inside the duct; the outer servo rotates the ring through a belt-pulley drive. **(B)** The belt-pulley drive moves the outer servo off the rotation axis, leaving the center open for wires. **(C)** Two angles describe the thrust direction: α_i, the rotation of the duct, and β_i, the rotation of the motor pair inside the duct. **(D)** Servo response to a $90°$ step command.

Gimbals. The gimbal mechanism enables each rotor system to rotate up to $\pm 1080^\circ$ along two perpendicular axes (Figure 3(A)), directing the rotor thrust on the sphere through three full revolutions from neutral (Figure 3(C)). This range is possible because we route the power and signal wires through an opening at the center of the outer servo rotation axis, and enable the resulting twist through slack along the wire length (Figure 3(B)). A belt-pulley transmission offsets the outer servo from the rotation axis, leaving the center clear for the pass-through; the inner servo sits inline with its axis and requires no such offset.[2]

Rotor systems. At the intersection of the two rotation axes of each gimbal, we mount a coaxial motor pair to provide thrust. Each propeller rotates in the opposite direction at equal speeds (Figure 3(A)). The counter-rotation benefits the thrust vectoring and controller design by eliminating two adverse effects that arise from a singular rotating propeller: (i) gyroscopic effect: a spinning rotor produces a precession torque that resists gimbal motion; and (ii) aerodynamic drag: a singular rotating propeller receives a reaction torque from the air along the spin axis that is inseparable from thrust generation. Without counter-rotation, the servo motors would need to overcome the dynamic load from (i) during thrust vectoring, and each rotor's thrust would couple with a torque from (ii). Furthermore, the aerodynamic drag would complicate MorphQuad's control and thrust allocation design, in a similar way to (*35*), preventing Enabler I. The dual-motor solution eliminates both the gyroscopic effect and the aerodynamic drag, leading to rapid and consistent servo motion (Figure 3(D)) and low-complexity thrust allocation.

Autonomy pipeline

We introduce a fully-onboard autonomy pipeline for MorphQuad, outlined in Figure 2(B). Co-designed with the hardware, the autonomy pipeline enables continuous omnidirectional vectoring of maximum thrust, almost-everywhere stable motion and force control, and fully-onboard localization without external motion capture or off-board computation. We inherit the standard PX4 quadrotor architecture and configure its perception, control, and thrust allocation modules for the

[2]Slip rings could be used instead to enable unlimited rotation along both axes.

localization and navigation of MorphQuad. The autonomy pipeline consists of four stages that translate the high-level setpoint commands into rotor and gimbal commands: (a) a trajectory planner that generates position and attitude trajectories based on the time-stamped setpoints we define along a path for a task; (b) a generalized geometric controller that computes the force and torque required for MorphQuad to track the planned trajectories; (c) an optimal thrust allocation that realizes the required force and torque by calculating the rotor speed and gimbal angles of each independently articulated rotor system; and (d) a state estimator that fuses camera and IMU measurements to enable localization in GPS-denied environments, free of a motion capture system.

Trajectory planner. We implement a trajectory planner to convert user-defined position and attitude setpoints into a smooth trajectory for MorphQuad to track since we design each task, including manipulations, with a series of time-stamped setpoints. In contrast to planners for regular quadrotors that consider coupled translation and rotation, our planner decouples them thanks to MorphQuad's ability to generate translational force at any orientation using independently articulated rotor systems. We use quintic-polynomial trajectories that guarantee continuous accelerations and smooth velocities (*62*) to connect the timed setpoints. We script the setpoints on the onboard companion computer (Jetson) and send the converted trajectory snapshots to the flight controller (Autopilot), in the form of reference states ($\boldsymbol{R}_d$, $\boldsymbol{\omega}_d$, $\boldsymbol{p}_d$, $\boldsymbol{v}_d$) at a frequency of $100\,\text{Hz}$.

Generalized geometric controller. Our generalized geometric controller computes the desired force and torque for MorphQuad to track the reference states provided by the trajectory planner; it leverages the omnidirectional thrust vectoring of MorphQuad to attract the vehicle to any arbitrary desired state. In contrast to a geometric controller on regular quadrotors (*63*) that only computes the thrust perpendicular to the body plane, we allow the geometric controller to independently command a thrust force spanning all three translational axes, on top of a torque spanning all three rotational axes. The generalization grants almost-everywhere exponential stability: MorphQuad can track trajectories across independent translation in $\mathbb{R}^3$, and at the same time, the rotation on the entire $\mathsf{SO}(3)$ manifold with only zero-measure exceptions, without the orientation-dependent

translation seen on regular quadrotors. We augment the generalized geometric controller with $\mathcal{L}_1$ adaptation (*64*); it allows MorphQuad to estimate and reject unmodeled disturbances from any direction by vectoring thrust in the counteracting direction of the disturbance in real time.[3] We derive the full generalized controller and adaptive law in the Materials and Methods section.

Thrust allocation. Our thrust allocation converts force and torque commands from the controller into the angular velocities (Ω_i) of the rotor systems, and the angular positions (α_i, β_i) of the gimbal servos. The allocation drives MorphQuad's four independently articulated rotor systems by solving a linear inversion that respects mechanical gimbal-lock and permits inter-rotor thrust cancellations to reduce downwash interference between rotors. We implement the allocation within the existing PX4 mixer framework, preserving compatibility with standard multirotor toolchains. We derive the full allocation in the Materials and Methods and prove its optimality in Supplementary Materials.

State estimation. Our state estimator provides state feedback of the vehicle's current position and orientation ($\boldsymbol{R}$, $\boldsymbol{\omega}$, $\boldsymbol{p}$, $\boldsymbol{v}$) at $800\,\text{Hz}$ by fusing visual-inertial odometry with inertial measurements using an Extended Kalman Filter. The state feedback enables the generalized geometric controller to compute the desired force and torque for trajectory tracking. We choose commercially available sensors, a stereo camera for visual-inertial odometry, and an off-the-shelf IMU suite, to maintain the compact standard design.

Experiment setup

We evaluate MorphQuad's co-designed hardware and autonomy in delivering maneuverability, manipulation, and resiliency (MMR). We design three groups of experiments (Figure 1): (a) maneuverability, where MorphQuad performs multi-revolution continual rotation and pointing, while

[3] On MorphQuad, $\mathcal{L}_1$ adaptation exploits that any external disturbance is *fully matched* due to MorphQuad's omnidirectional thrust vectoring (*65*). Alternative methods include Incremental Nonlinear Dynamic Inversion (*66*), for high-agility maneuvering, and simultaneous system identification and model predictive control, for constraint-aware and mode-shifting (*e.g.*, from free flight to in-contact flight) task execution (*67*).

either translating to inspect a pipe, or hovering to track a hand movement; (b) manipulation, where MorphQuad turns a valve, nails a target, and pushes an object through contact-based force application; and (c) resiliency, where MorphQuad rejects winds and physical-displacement disturbances. MorphQuad completes all tasks with fully-onboard autonomy pipeline without motion capture, GPS, or off-board computations. We next introduce the setup of each task, including objects in the environment, additional onboard equipment, and external devices. Then, we elaborate the evaluation metrics and an overview of MorphQuad's performance in these experiments.

Maneuverability experiments. The pipe-inspection workspace contains two horizontal parallel pipes (Figure 4(A)) with a vertical gap of 1.3 times MorphQuad's side length, forcing tight position tracking for collision-free traversal. The hand-tracking workspace has a human operator standing 1.5 m in front of MorphQuad (Figure 4(B)); the operator extends one hand toward MorphQuad's onboard camera, and MorphQuad hovers in place, tracking the hand's pointing direction and matching its roll tilt in real time while the operator moves the hand.

Manipulation experiments. For the valve-turning task, we mount a valve on a wall 3 m above the ground, with its 30 cm-long axis extruding outward at 45° from the wall (Figure 5(A)); such a valve would otherwise require a human operator on a ladder to operate. We equip MorphQuad with a rigid "Y"-shaped passive end-effector at its front that enters the valve's spokes to turn it. For perching and nailing, we mount a styrofoam block on a wall 2 m above the ground; we attach a nail perpendicularly to MorphQuad's bottom via a neodymium magnetic connector that releases cleanly after insertion (Figure 5(B)). For pushing, we place a wheeled whiteboard weighing 30 kg unrestrained on the floor (Figure 5(C)); MorphQuad needs to perch on the whiteboard to push it.

Resiliency experiments. For wind disturbances, we direct a leaf blower at MorphQuad with its nozzle within 30 cm of MorphQuad's front face, producing an airflow of 30 m/s measured at the same front face (Figure 6(A)). Unlike a wind tunnel (*18*) or fan array (*61*) that generates a uniform freestream, this setup concentrates peak airflow at a small incidence area, producing spatially non-

uniform and time-varying force and torque disturbances that simultaneously load translation and rotation —a regime distinct from, not easier than, a uniform freestream. For impulsive physical displacements, a human operator wields a hammer to apply the physical displacement; the hammer head makes direct contact with MorphQuad's body, producing lateral pushes and off-centered picks (Figure 6(B)). For sustained disturbances, the operator applies a pulling force via a tether connected to MorphQuad through an inline force meter (Figure 6(C)).

Task implementation and evaluation metric. We define task-specific setpoints of each task for the trajectory planner and record position and orientation tracking errors throughout. Because MorphQuad achieves localization from onboard visual-inertial odometry, we report all tracking errors in the world frame as estimated by the onboard state estimator. We do not evaluate the accuracy of contact force and torque since neither the trajectory planner commands contact force or torque, nor is the vehicle equipped with the necessary sensors. Specifically, for manipulation tasks, MorphQuad relies on position and attitude references by the planner, and maintains accurate trajectory tracking, upon treating any counteracting forces and torques as disturbances.

Evaluation summary. **(a) Maneuverability**: MorphQuad demonstrates simultaneous rotation and translation, including 720° continual rotation that is unprecedented on previous variable-tilt multirotors. The trajectory tracking maintains a position RMSE below 6 cm and orientation RMSE below 5°. **(b) Manipulation**: MorphQuad demonstrates omnidirectional force and torque application, including a lateral force generation comparable to its takeoff mass (4.56 kg) and its torque application comparable to a human wrist (4.92 Nm). Upon the completion of tasks, we report a position RMSE below 5 cm and an attitude RMSE below 3° along axes that are not affected by the interaction. **(c) Resiliency**: MorphQuad maintains similar motion accuracy across different hovering attitudes amid winds and push/pull/pick disturbances, even when a 30 m/s wind gust is directly fed to one of its propellers. MorphQuad achieves a position RMSE of approximately 8 cm along the dominant wind axis, and the orientation RMSE below 5°. MorphQuad maintains its position RMSE 2–4 cm and orientation RMSE below 5° on axes orthogonal to physical displacements.

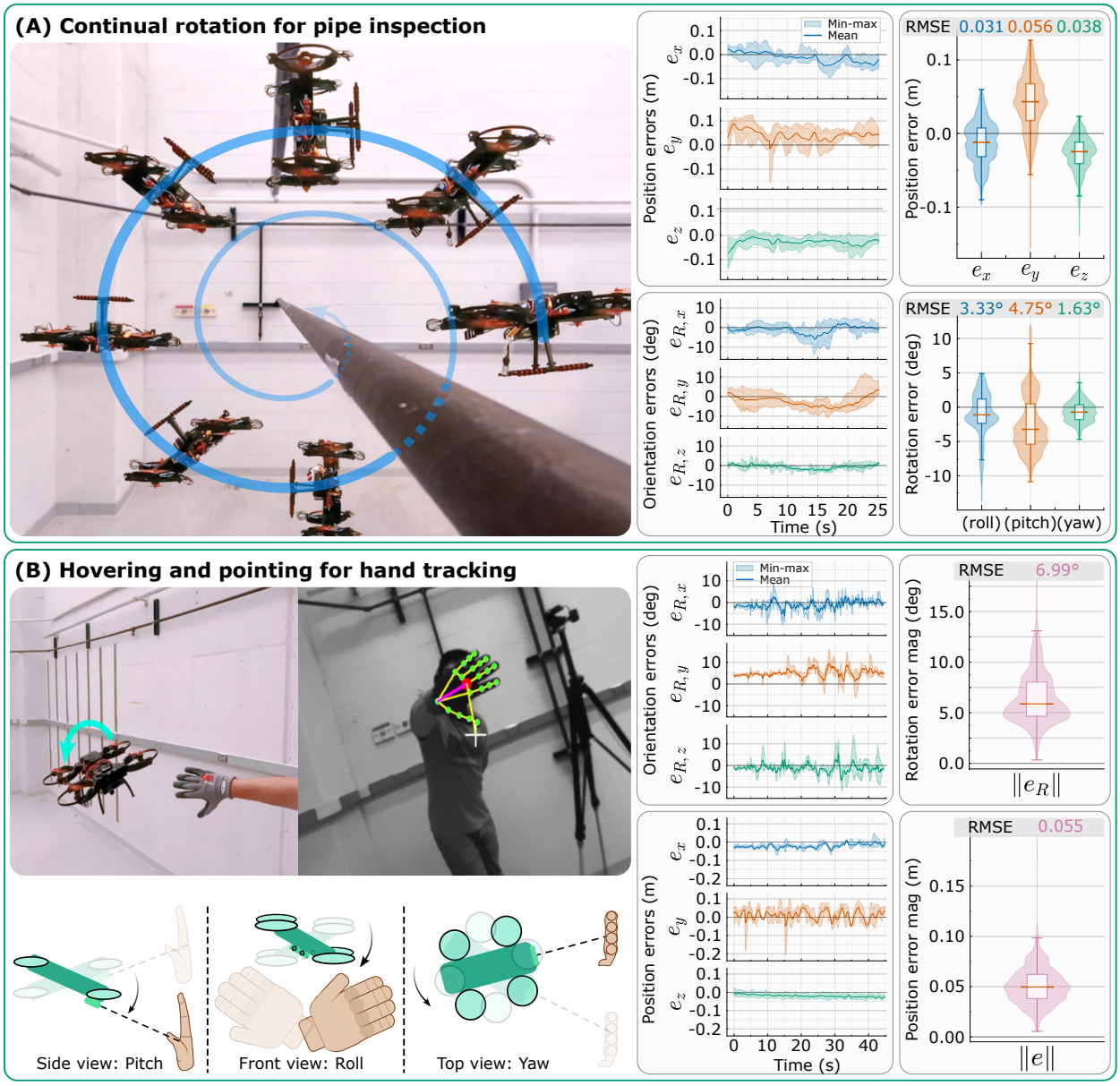

Figure 4: Maneuverability experiments. **(A)** Continual rotation during pipe inspection: MorphQuad rotates around a pipe continually for 720° following a circular translation trajectory, its heading direction always pointing at the pipe. **(B)** Hovering and pointing for hand tracking: MorphQuad tracks a human operator's hand orientation from a fixed hover point using onboard vision, independently commanding roll, pitch, and yaw while maintaining position.

Maneuverability: Simultaneous translation and multi-revolution rotation

We demonstrate MorphQuad's motion stability and accuracy during omnidirectional flight, including simultaneous translation and multi-revolution rotation, unprecedented on previous variable-tilt multirotors. In particular, MorphQuad performs (a) pipe inspection via a continual 720° pitch rotation around a pipe while keeping the heading direction towards the pipe; it emulates practical maintenance applications where the robot needs to traverse between pipes and keep onboard sensors pointing towards a target and (b) real-time hand tracking using onboard vision while hovering; it showcases MorphQuad's quick and accurate response to dynamic and unpredictable target states.

Continual rotation for pipe inspection

MorphQuad executes the pipe-inspection task by simultaneously translating along a circle with a $1\,\text{m}$ diameter in a vertical plane around a horizontal pipe and pitching 720° continually, as shown in Figure 4(A). The narrow inter-pipe gap demands accurate position tracking for collision-free operation despite the excessive rotation. MorphQuad achieves position errors below $6\,\text{cm}$ RMSE on all three axes and pitch errors at 5.5° RMSE across the full trajectory. The demonstration of simultaneous multi-revolution continual rotation during translation is unprecedented on previous variable-tilt multirotors, demonstrating its maneuverability.

Hovering and pointing for hand tracking

Dynamic and unpredictable setpoints challenge the controller and hardware under conditions closer to real-world pointing tasks than pre-scripted trajectories (Figure 4(B)). We implement an onboard hand-orientation detector to estimate the operator's hand pose from the front camera feed and send orientation setpoints to the flight controller, so that MorphQuad follows the hand pose: pitch and yaw authority allow the vehicle to point in any direction, effectively sweeping the camera over a full sphere, while roll commands keep the hand upright in the camera frame.

Despite the dynamic hand movements, MorphQuad maintains a position RMSE of $5.5\,\text{cm}$ during hand tracking, confirming that the position controller remains decoupled from the orientation

commands even under reactive setpoints. The orientation tracking RMSE is 6.99°, with the error distribution concentrated between approximately 3° and 8°. Occasional outliers exceeding 15° correspond to rapid hand accelerations that momentarily saturate the visual servo reaction, accounting for the higher orientation error relative to experiment (a).

Manipulation: Turning valves, perching and nailing, and pushing objects

We demonstrate MorphQuad's capability of force and torque application —at a similar level to a human wrist— in arbitrary directions. In particular, we design three tasks of distinct objectives (Figure 5): (a) Turning a valve wheel; it requires torque application on top of motion control. (b) Perching on a wall and pressing a nail into a surface; it requires sustained directional force application on top of motion control. (c) Pushing a heavy wheeled object; it requires sustained force application against an unrestrained moving surface, challenging the control resiliency. We remark that all manipulation tasks remain open-loop with respect to contact: MorphQuad uses neither force/torque sensors, nor visual servoing during manipulation; instead, the trajectory planner only prescribes position and attitude setpoints. The vehicle follows the smooth trajectory that connects the setpoints upon treating all counteracting contact forces and torques as disturbances.

Valve turning

MorphQuad approaches the valve at a 45° pitch to align the end-effector with the spokes of the valve wheel. Once engaged, MorphQuad locks its position and rotates about the valve axis to complete the turning, as shown in Figure 5(A). As wheeled valves are common infrastructure control mechanisms, this task highlights the potential of MorphQuad in maintenance automation.

During task execution, MorphQuad simultaneously holds position and rolls aligned with the valve axis to generate a torque that rotates the wheel. The experiment is demanding since MorphQuad operates close to the wall, on top of the unknown torque needed to turn the valve, the aerodynamic wall effects perturb the airflow and risk the position control accuracy; consequently, a high position error would cause collision between MorphQuad and the surrounding structures.

Despite the challenges, MorphQuad maintains position control throughout the valve turning maneuver, with position RMSE at 4 cm along the z-axis and below 3 cm along the x- and y-axes. Orientation RMSEs are 3.9° in roll, 7.7° in pitch, and 2.4° in yaw. We attribute the elevated pitch error to the added mass of the front-mounted end-effector: the added mass induces a nose-down moment not directly accounted for in the geometric controller since we employ MorphQuad's nominal model without the front-mounted end-effector. We record a maximum body torque of 4.92 Nm in pitch (and by symmetry in roll) during hover, confirming that the rotor system delivers torque authority that is comparable to human wrists (*59*) and satisfies industrial specifications (*60*).

Perching and nailing

MorphQuad approaches the wall while continuously rotating its body, transitioning from nominal hover to a wall-parallel pose; once the nail aligns with the target, the controller applies a sustained force toward the wall to perch and press the nail into the styrofoam, as shown in Figure 5(B); finally, MorphQuad moves up to break the magnetic connection and retreats from the wall. This task demonstrates the application of a sustained force while holding an arbitrary pose that promises MorphQuad in versatile manipulation.

MorphQuad maintains a tracking error similar to hover during the approach and rotation phase (Figure 5(B)). Upon contact, noticeable oscillation appears as the nail resists insertion. We attribute this oscillation to (i) compliance in the landing legs leads to vibration at impact with the wall, and (ii) the close proximity of the propellers to the wall induces turbulence that disturbs the rotor thrust. Despite these disturbances, the overall position RMSE remains approximately 5 cm across all three axes, with orientation RMSEs of 2.4°, 2.9°, and 2.3° in roll, pitch, and yaw, respectively.

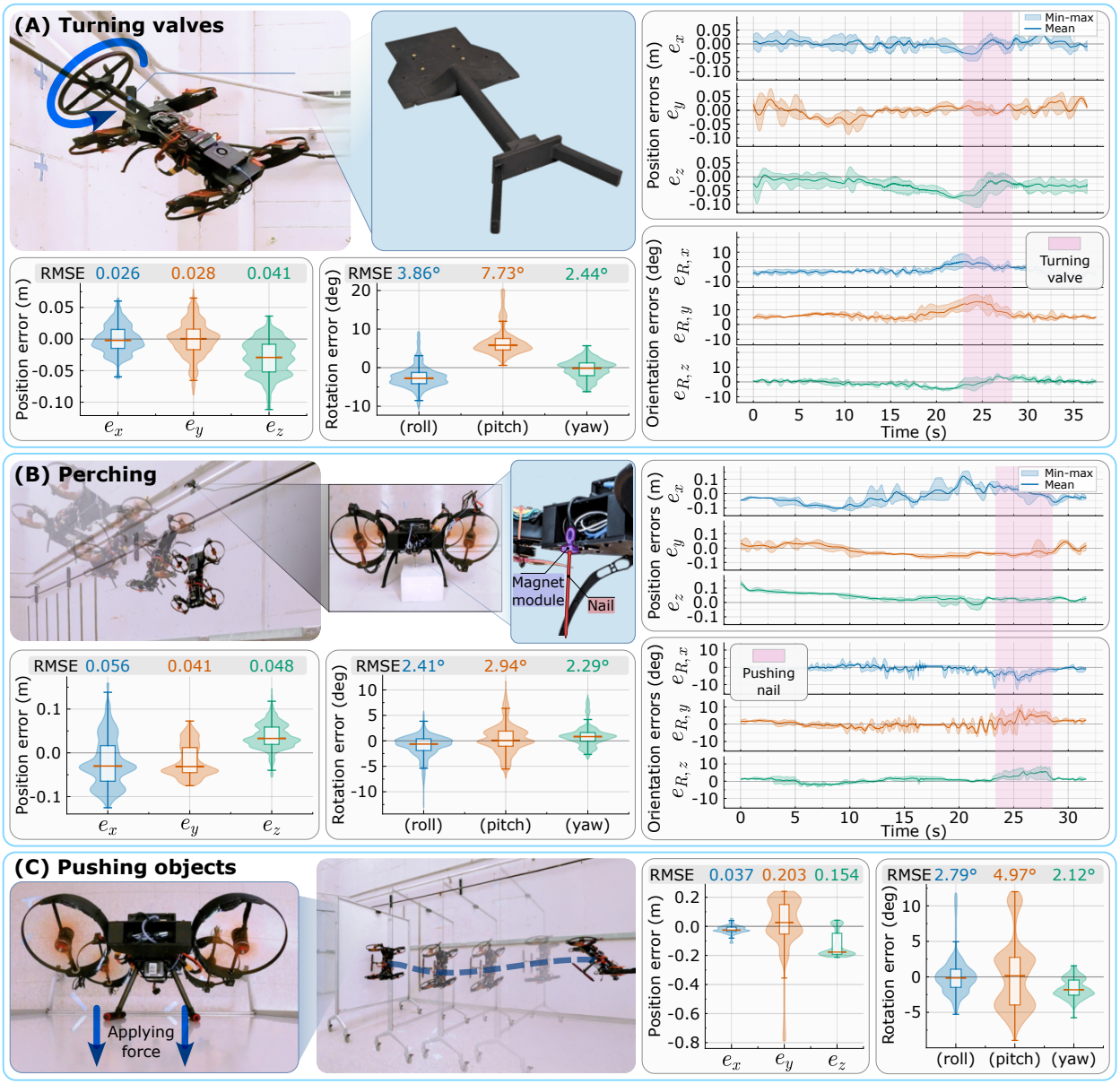

Figure 5: Manipulation experiments. **(A)** Valve turning: MorphQuad approaches a wall-mounted valve and rotates the wheel by generating body torque. **(B)** Perching and nailing: MorphQuad transitions from nominal hover to a wall-parallel pose and presses a magnetically attached nail into a styrofoam target. **(C)** Pushing objects: MorphQuad perches onto a wheeled whiteboard and displaces it across the floor.

Pushing objects

We task MorphQuad to push the whiteboard across the floor for around 1 m (Figure 5(C)), emulating a door-opening or obstacle-clearing action in search-and-rescue. Unlike pressing against a rigid wall, MorphQuad perches onto the whiteboard and drives it across the floor, requiring the controller to maintain consistent contact against a surface that moves. Wall effects persist throughout the interaction. Because the manipulation pipeline currently operates without feedback on contact force, we feedforward a constant body-frame acceleration after perching to sustain the push.

We report, in Figure 5(C), a noticeably higher position error along the y-axis than in other experiments. Since MorphQuad converts the desired pushing force into a constant body-frame acceleration without updating the position setpoint, the approximately 0.8 m of board displacement accumulates directly as reported y-axis error. The remaining axes exhibit considerably smaller errors, with x-axis RMSE at approximately 3 cm and z-axis RMSE at roughly 15 cm. We attribute the elevated z-axis error to intensified wall effects and contact friction from sustained close proximity to the whiteboard surface. The controller maintains stable attitude tracking throughout the push, with orientation RMSEs of approximately 2.8° in roll, 5.0° in pitch, and 2.1° in yaw, confirming that sustained contact does not compromise attitude stability.

Resiliency: Disturbance rejection under winds and physical displacements

We demonstrate MorphQuad's resilient operation under challenging disturbances —including a 30 m/s (67 mph or 108 km/h) wind stream directed into a single rotor system, applied across multiple hover attitudes. In particular, we design three types of disturbances that span real-world flight (Figure 6): (a) Hovering at different attitudes under sustained winds from time-varying directions; it demonstrates MorphQuad's control resiliency under aerodynamic disturbances, the most common real-world stressor for aerial vehicles. (b) Impulsive push and pick disturbances; it demonstrates transient recovery from collisions and the decoupling of translational and rotational control. (c) Sustained tethered pull; it demonstrates motion accuracy under continuous load.

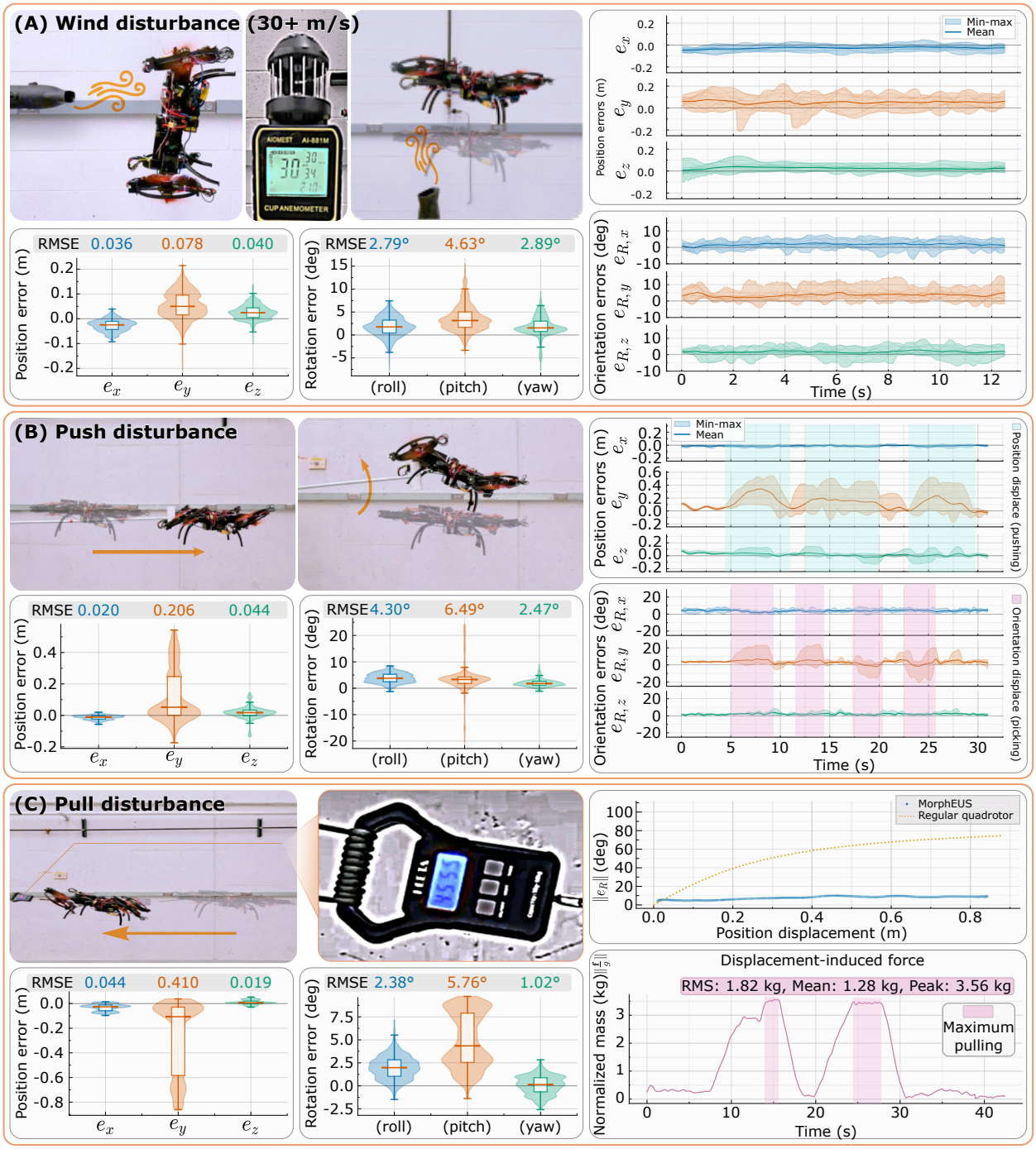

Figure 6: Resiliency experiments. **(A)** Wind: MorphQuad holds a hover setpoint under time-varying leaf-blower output. **(B)** Push and pick: MorphQuad endures impulsive translational and rotational displacements. **(C)** Pull: MorphQuad reacts to sustained pulling force.

Strong varying wind fields

We design four hover scenarios that span the range of real-world wind encounters: abrupt onset from an off-axis direction, periodic sweeping across the front face of MorphQuad, abrupt onset while the quadrotor hovers in a vertical (90° pitch) pose exposing its full lateral cross-section (Figure 6(A)), and direct blowing into a single propeller creating highly asymmetric aerodynamic interference. We sustain each scenario for 30 seconds while MorphQuad hovers at a fixed setpoint.

MorphQuad maintains stable hovering at different attitudes despite the winds. Because the wind is predominantly oriented along the y-axis of MorphQuad, the largest positional displacement appears in that direction with an RMSE of approximately 8 cm, while the x- and z-axes remain closer to 4 cm. The controller maintains strong attitude tracking throughout, with orientation RMSEs of 2.8° in roll, 4.6° in pitch, and 2.9° in yaw. These results validate the flight resiliency of MorphQuad under unknown, strong, and time-varying aerodynamic disturbances.

Impulsive push and pick disturbances

We evaluate MorphQuad's ability to recover from sudden displacements by applying disturbances at irregular intervals. We apply two types of disturbances: lateral pushes to the quadrotor body that induce translational displacements, and off-centered vertical pushes from below (picks) that simultaneously displace MorphQuad and impart a rotational disturbance. Physical collisions are an unavoidable reality in cluttered environments and during contact-based tasks.

Push disturbances along the y-axis displace the quadrotor by as much as 50 cm from its setpoint (Figure 6(B)). Despite these large translational excursions, the controller holds the orthogonal axes with errors comparable to maneuver tasks (x-axis RMSE: 2 cm; z-axis: 4 cm). Similarly, although pitch reaches over 20° of disturbance in both directions, the controller maintains roll and yaw at 4.3° and 2.5° RMSE, respectively. The time-series data confirm decoupled recovery: large positional displacements do not propagate into rotational errors, and large rotational disturbances do not degrade translational tracking.

Sustained pull disturbances

We quantify MorphQuad's maximum disturbance rejection capability by subjecting it to sustained pulling forces. The operator gradually increases the tension until MorphQuad reaches its maximum sustainable resistance. The force sensor records a peak load of 4.55 kg, while the disturbance force estimated from the position error and controller state reaches 3.56 kg. The 0.99 kg discrepancy between the two measurements is attributed to online disturbance rejection that counteracts a portion of the pulling force before it manifests as position error.

Consistent with the push disturbance results, a large y-axis displacement exceeding 80 cm does not propagate into the orthogonal axes (Figure 6(C)): the x-axis RMSE remains at 4.4 cm and the z-axis at 2 cm, while the controller holds roll and yaw at 2.4° and 1.0°, respectively. The pitch RMSE of 5.8° reflects the slight upward angle of the tether pull.

We contextualize this result through a scatter plot in Figure 6(C) comparing the rotational error induced by translational displacement for MorphQuad against a simulated standard quadrotor under identical tether loading conditions. For MorphQuad, increasing positional displacement produces virtually no growth in rotation error, confirming decoupled disturbance rejection. The simulated conventional quadrotor exhibits rapidly growing rotation error with displacement because it must pitch or roll to generate the lateral thrust needed to counteract the positional disturbance. This comparison quantitatively illustrates a fundamental advantage of MorphQuad's independently articulated rotor architecture: MorphQuad rejects external forces through independent thrust vectoring, whereas a standard quadrotor suffers coupled translational and rotational responses.

Discussion

Summary of results. MorphQuad is the first omnidirectional multirotor aerial vehicle to simultaneously achieve Enablers I–III. We validate MorphQuad, with fully-onboard autonomy, in MMR experiments. **(a) Maneuverability:** MorphQuad rotates continuously beyond 360° while translating around pipes, and points while hovering to track a hand. **(b) Manipulation:** MorphQuad generates torque of 4.92 Nm and lateral force of 4.55 kg on top of hovering —comparable to a human wrist (*59*) and sufficient for industrial tasks (*60*)— enabling it to turn an inclined valve, perch on a wall to press a nail, and push heavy objects. **(c) Resiliency:** MorphQuad holds against 30 m/s wind from any direction —including wind directed into a single rotor system— impulsive pushes, and sustained pulls. Across all tasks, MorphQuad holds position within 2–5 cm and orientation within 3–6° along undisturbed axes.

Significance. MorphQuad promises to enable autonomous infrastructure maintenance, contact-based inspection, and emergency response with a single aerial platform. **Infrastructure inspection and maintenance**: The pipe inspection demonstrates the simultaneous translation and beyond-360° rotation needed for practical infrastructure inspection. The valve turning demonstrates the human-level torque needed to operate industrial mechanisms at hard-to-reach sites as both workflows today rely on scaffolding, rope access, or a human operator on a ladder. **Contact-based inspection**: The perching-and-nailing demonstrates the sustained directional human-level force needed to press sensors against infrastructure surfaces for integrity assessment, regardless of surface orientation. **Emergency response**: The object pushing, alongside resilience to wind, impulsive pushes, and sustained pulls, demonstrates the obstacle-clearing capacity comparable to a human wrist; it also demonstrates disturbance robustness needed in cluttered, wind-exposed, and collapsed environments. All results are obtained with fully on-board sensing and computation — no motion capture, no GPS, no off-board compute— removing the constraint that has confined prior omnidirectional multirotor demonstrations to laboratory settings, and aligning MorphQuad with the unstructured environments these applications demand.

Future work. We will extend MorphQuad along (a) robust, adaptive, and agile flight, (b) force-aware physical interaction, and (c) natural-language control. **(a) Robust, adaptive, and agile flight**: adding LiDAR-based SLAM (*68, 69*) to enhance MorphQuad's fully-onboard autonomy would let it navigate robustly across low-light, cluttered environments where cameras alone struggle. Combining online system identification with model-predictive control (*67*) would provide MorphQuad with adaptive transitions between free flight and in-contact flight. Explicitly modeling the dynamics of motors and servos, for example through incremental nonlinear dynamic inversion (INDI) (*66*), could sharpen the responsiveness of thrust vectoring and push MorphQuad toward acrobatic-level maneuvers. **(b) Force-aware physical interaction**: MorphQuad's resiliency already absorbs contact forces. Adding end-effector force and torque sensing (*3*) together with soft manipulators (*70*) would allow precise interaction, enabling delicate aerial tasks such as inspection, assembly, and contact-rich maintenance. **(c) Natural-language control**: integrating vision-language-action models (*71*) would bring foundation-model manipulation —common in fixed-base robotic arms— into the air, letting operators direct MorphQuad through natural language.

Materials and Methods

We present the mechatronic components, dynamics, and control framework that enable MorphQuad to realize vectoring of maximum thrust in any direction and almost-global stability on a compact quadrotor design with fully onboard autonomy. We first identify the mechatronic components of the vehicle structure, actuation, and onboard computing, then derive the translational and rotational dynamics of MorphQuad, and finally present the three-layer control architecture: a geometric controller for singularity-free trajectory tracking on $\mathsf{SE}(3)$, an $\mathcal{L}_1$ adaptive augmentation for disturbance compensation, and a null-space-aware thrust allocation that resolves inter-rotor aerodynamic interference and gimbal lock. Together, these components translate high-level $\mathsf{SE}(3)$ trajectory commands into individual rotor speeds and gimbal angles that demonstrate MorphQuad's maneuverability, manipulation, and resiliency.

Mechatronic design

Main body. We preserve the compact footprint of a conventional quadrotor by arranging the four rotor systems in an H-configuration on a main body composed of two parallel carbon-fiber-infused PLA plates (Figure 2(A)). The dual-plate design serves a structural and organizational role: the ESCs and power distribution electronics sit protected between the plates, the top plate houses the flight and task computers, and the bottom plate mounts the camera for visual-inertial odometry. This arrangement retains the geometric profile needed to access confined and narrow environments while housing the full actuation, sensing, and computation required for omnidirectional flight. The takeoff mass, including batteries, is $4.56\,\text{kg}$, and all electronic and mechanical components are commercially available off-the-shelf products.

Rotor systems. Each rotor system pairs two coaxial counter-rotating rotors with a two-axis gimbal (Figure 3(A)): the counter-rotating pair cancels rotor-induced drag torque and gyroscopic precession, and the gimbal orients the pair to direct thrust in any direction. Each gimbal axis is driven by a DYNAMIXEL servo selected for its compact form factor and position feedback —XL330-

M288-T on the inner axis, XC330-M288-T on the outer— and the eight servos daisy-chain over a single UART bus to the flight computer. Each coaxial pair consists of two brushless T-Motor VELOX 3008 1500KV motors driving 6-inch triple-blade propellers, sized for a rotor-pair thrust of $2.8\,\text{kg}$ that lets MorphQuad hover at 40% throttle. Peak motor draw exceeds $43.6\,\text{A}$ during fast maneuvers, which sets our choice of independent ESCs rated at $51\,\text{A}$ continuous current.

Computing and simulation. The onboard computing stack enables fully-onboard autonomy without off-board compute or motion capture: a Pixhawk Autopilot FMUv6x flight controller runs attitude and position control, an NVIDIA Jetson Orin Nano runs trajectory generation, and an Intel RealSense stereo-vision depth camera supplies the VIO sensor stream (*72, 73*). To validate the full software stack prior to hardware deployment, we integrate MorphQuad's structural, kinematic, and dynamic models into a ROS and Gazebo software-in-the-loop (SITL) simulator.

Vehicle Dynamics

The omnidirectional maximum thrust vectoring capability of MorphQuad originates from the gimbal-mounted coaxial rotor systems, whose servo-driven tilt angles appear directly in the equations of motion. We define four coordinate frames for the derivation: the world frame $\mathcal{W}$, the body-fixed frame $\mathcal{B}$, and a propeller-fixed frame $\mathcal{P}_i$ for each rotor arm $i \in \{1, 2, 3, 4\}$. The frame conventions and servo angles are shown in Figure 7. By design, the $\mathcal{B}$-to-$\mathcal{P}_i$ transformation is parameterized by two servo positions: α_i controlled by the inner servo and β_i by the outer servo, as shown in Figure 3(C) and Figure 7. These servo angles provide additional actuator commands alongside the propeller speeds, giving MorphQuad a total of twelve independent control inputs.

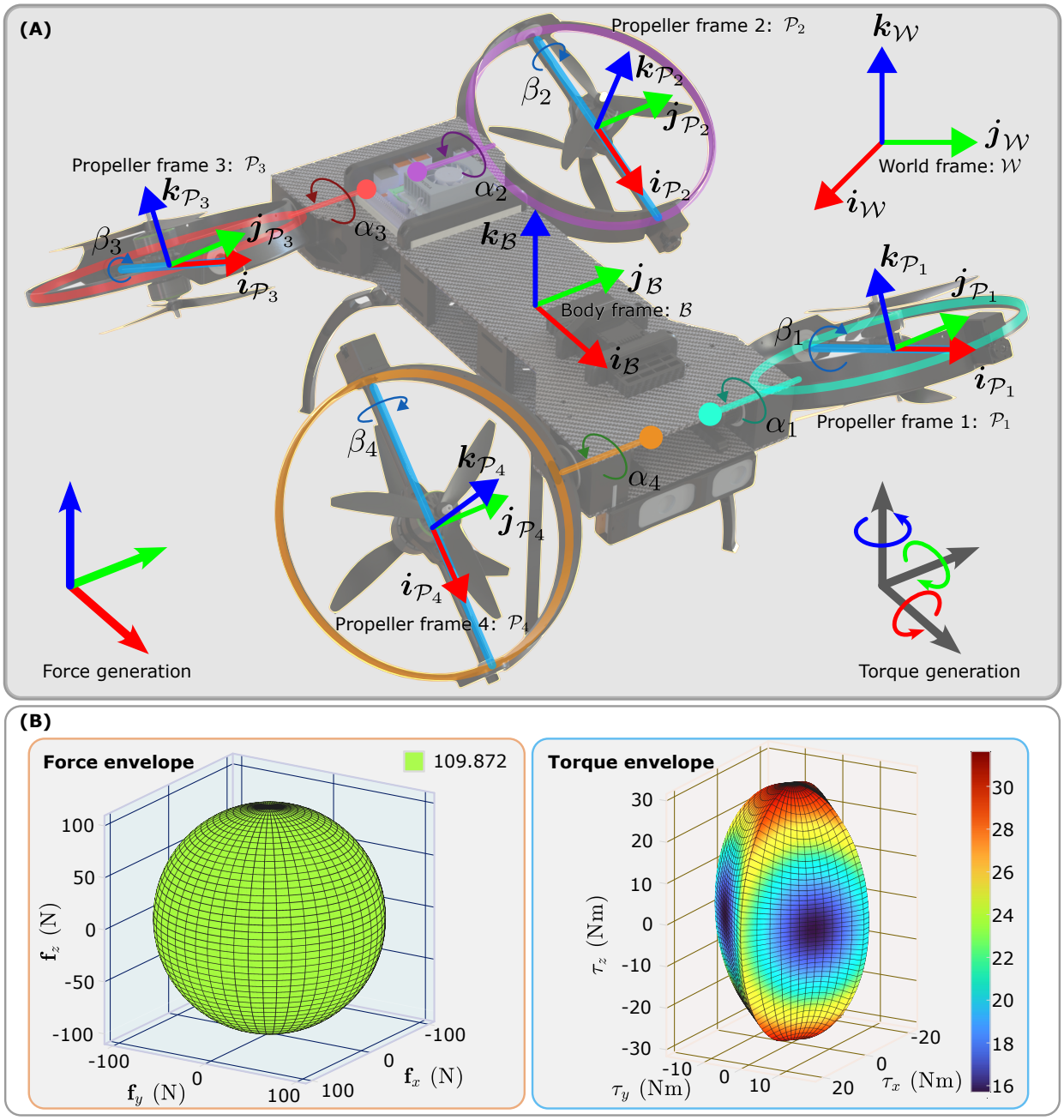

Figure 7: **(A)** Schematic of the quadrotor highlighting coordinate frames and servo angles. **(B)** Force and torque envelopes of MorphQuad, assuming that each arm can apply a maximum thrust of $24.5\,\mathrm{N}$. Force envelope assumes desired torque to be zero, and vice versa. Both envelopes are obtained assuming no thrust cancellation enabled for inter-rotor downwash avoidance.

The translational dynamics are

$$\dot{\boldsymbol{p}} = \boldsymbol{v}, \quad m\dot{\boldsymbol{v}} = m\boldsymbol{g} + \boldsymbol{R}\boldsymbol{f}, \tag{1}$$

where $\boldsymbol{p} \in \mathbb{R}^3$ and $\boldsymbol{v} \in \mathbb{R}^3$ are position and velocity in $\mathcal{W}$, m is the quadrotor mass, $\boldsymbol{g} \in \mathbb{R}^3$ is the gravitational acceleration in $\mathcal{W}$, $\boldsymbol{R} \in \mathsf{SO}(3)$ is the rotation matrix from $\mathcal{B}$ to $\mathcal{W}$, and $\boldsymbol{f} \in \mathbb{R}^3$ is the total propeller force in $\mathcal{B}$.

The gimbal design enables the generation of rotor thrust, and thus the body forces $\boldsymbol{f}$, in any direction. Each rotor system produces a vectorized thrust whose direction is set by the servo angles α_i, β_i and whose magnitude scales with the propeller angular velocity Ω_i. The body-frame force is

$$\boldsymbol{f} = \sum_{i=1}^{4} \boldsymbol{t}_i = c_t \sum_{i=1}^{4} \boldsymbol{G}_i(\alpha_i, \beta_i)\, \Omega_i^2, \tag{2}$$

where c_t is the thrust coefficient and the thrust direction vector

$$\boldsymbol{G}_i(\alpha_i, \beta_i) = \begin{bmatrix} \sin\alpha_i \cos\beta_i \\ -\sin\beta_i \\ \cos\alpha_i \cos\beta_i \end{bmatrix} \tag{3}$$

results from two intrinsic rotations of the gimbal: first by α_i about the $\boldsymbol{j}_{\mathcal{B}}$ axis (inner servo), then by β_i about the rotated $\boldsymbol{i}_{\mathcal{B}}$ axis (outer servo), as shown in Figure 7.

The rotational dynamics follow Euler's equations,

$$\dot{\boldsymbol{R}} = \boldsymbol{R}[\boldsymbol{\omega}]_\times, \quad \boldsymbol{J}\dot{\boldsymbol{\omega}} = -\boldsymbol{\omega} \times \boldsymbol{J}\boldsymbol{\omega} + \boldsymbol{\tau}, \tag{4}$$

where $\boldsymbol{\omega} \in \mathbb{R}^3$ is the angular velocity in $\mathcal{B}$, $[\cdot]_\times : \mathbb{R}^3 \to \mathbb{R}^{3\times3}$ is the skew-symmetric matrix operator, $\boldsymbol{J} \in \mathbb{R}^{3\times3}$ is the inertia matrix in $\mathcal{B}$, and $\boldsymbol{\tau} \in \mathbb{R}^3$ is the propeller torque in $\mathcal{B}$.

A key advantage of the coaxial design is that each pair of counter-rotating propellers cancels the aerodynamic drag torque and eliminates the gyroscopic reaction that would otherwise resist gimbal motion. The servos can therefore redirect thrust using minimal effort, and the net torque on the body reduces to the moment of each thrust vector about the center of mass (COM),

$$\boldsymbol{\tau} = \sum_{i=1}^{4} \boldsymbol{l}_i \times \boldsymbol{t}_i, \tag{5}$$

where $\boldsymbol{l}_i = [l_{i,x},\, l_{i,y},\, l_{i,z}]^\top$ is the position vector from the COM to the center of propeller i, and $\boldsymbol{t}_i = c_t \boldsymbol{G}_i(\alpha_i, \beta_i)\, \Omega_i^2$ is the thrust of propeller i in $\mathcal{B}$. Substituting yields

$$\boldsymbol{\tau} = c_t \sum_{i=1}^{4} \boldsymbol{H}_i(\alpha_i, \beta_i)\, \Omega_i^2, \tag{6}$$

where

$$\boldsymbol{H}_i(\alpha_i, \beta_i) = \begin{bmatrix} l_{i,y} \cos\alpha_i \cos\beta_i + l_{i,z} \sin\beta_i \\ -l_{i,x} \cos\alpha_i \cos\beta_i + l_{i,z} \sin\alpha_i \cos\beta_i \\ -l_{i,x} \sin\beta_i - l_{i,y} \sin\alpha_i \cos\beta_i \end{bmatrix}. \tag{7}$$

Combining the force (2) and torque (6) expressions gives the full wrench,

$$\boldsymbol{w} = c_t \sum_{i=1}^{4} \begin{bmatrix} \boldsymbol{G}_i(\alpha_i, \beta_i) \\ \boldsymbol{H}_i(\alpha_i, \beta_i) \end{bmatrix} \Omega_i^2 = c_t \boldsymbol{F} \boldsymbol{\Omega}^{\circ 2}, \tag{8}$$

where $\boldsymbol{w} = [\boldsymbol{f}^\top \;\; \boldsymbol{\tau}^\top]^\top \in \mathbb{R}^6$ is the stacked force-torque vector, $\boldsymbol{F}(\boldsymbol{\alpha}, \boldsymbol{\beta}) \in \mathbb{R}^{6\times 4}$ stacks the per-rotor wrench-direction vectors $[\boldsymbol{G}_i^\top \;\; \boldsymbol{H}_i^\top]^\top$ as columns, $\boldsymbol{\Omega} = [\Omega_1 \;\; \Omega_2 \;\; \Omega_3 \;\; \Omega_4]^\top$, and $(\cdot)^{\circ 2}$ denotes the element-wise square.

For control design, it is convenient to treat the individual thrust vectors $\boldsymbol{t}_i \in \mathbb{R}^3$ as abstracted inputs rather than the rotor speeds Ω_i. Stacking all four thrust vectors into $\boldsymbol{t} = [\boldsymbol{t}_1^\top \;\; \boldsymbol{t}_2^\top \;\; \boldsymbol{t}_3^\top \;\; \boldsymbol{t}_4^\top]^\top \in \mathbb{R}^{12}$, the wrench can be written in compact form as

$$\boldsymbol{w} = \boldsymbol{M}\boldsymbol{t}, \tag{9}$$

where $\boldsymbol{M} \in \mathbb{R}^{6\times 12}$ is a constant matrix determined by the fixed rotor positions $\boldsymbol{l}_i$ in $\mathcal{B}$. Since the matrix is wide and always full row-rank, the input has control over all wrench channels: the actuators can always produce a compensating input in the same subspace as an external force and torque disturbance, i.e., every disturbance is matched. In addition, $\boldsymbol{M}$ also serves as the basis for the thrust allocation described below.

Control

The central capability of MorphQuad is the independent generation of forces and torques in all six degrees of freedom, enabling omnidirectional trajectory tracking in $\mathsf{SE}(3)$. This section describes the three-layer control architecture: a geometric controller that tracks desired trajectories

on $\mathsf{SE}(3)$ (*63*), an $\mathcal{L}_1$ adaptive augmentation that compensates for unknown disturbances (*64*), and a thrust allocation strategy that converts desired wrenches into rotor commands while maximizing hovering efficiency and avoiding actuation deficiencies.

Geometric controller

The geometric controller computes desired body-frame force and torque from tracking errors defined directly on the $\mathsf{SE}(3)$ manifold, avoiding the singularities inherent in Euler angle representations. The tracking errors consist of two configuration-level errors and two rate-level errors,

$$\begin{aligned} \boldsymbol{e}_{\boldsymbol{p}} &= \boldsymbol{p} - \boldsymbol{p}_d, && \text{(position error)} \\ \boldsymbol{e}_{\boldsymbol{R}} &= \frac{1}{2}\left(\boldsymbol{R}_d^\top \boldsymbol{R} - \boldsymbol{R}^\top \boldsymbol{R}_d\right)^\vee, && \text{(orientation error)} \\ \boldsymbol{e}_{\boldsymbol{v}} &= \boldsymbol{v} - \boldsymbol{v}_d, && \text{(linear velocity error)} \\ \boldsymbol{e}_{\boldsymbol{\omega}} &= \boldsymbol{\omega} - \boldsymbol{R}^\top \boldsymbol{R}_d\, \boldsymbol{\omega}_d, && \text{(angular velocity error)} \end{aligned} \tag{10}$$

where $\boldsymbol{p}_d$, $\boldsymbol{v}_d$, $\boldsymbol{R}_d$, $\boldsymbol{\omega}_d$ are the desired position, velocity, rotation matrix, and angular velocity, and $(\cdot)^\vee : \mathfrak{so}(3) \to \mathbb{R}^3$ is the map that extracts a 3D vector from a skew-symmetric matrix.

The desired force and torque are

$$\begin{aligned} \boldsymbol{f}_{\text{Geo}} &= \boldsymbol{R}^\top \left(-k_{\boldsymbol{p}}\boldsymbol{e}_{\boldsymbol{p}} - k_{\boldsymbol{v}}\boldsymbol{e}_{\boldsymbol{v}} - m\boldsymbol{g} + m\ddot{\boldsymbol{p}}_d\right), \\ \boldsymbol{\tau}_{\text{Geo}} &= -k_{\boldsymbol{R}}\boldsymbol{e}_{\boldsymbol{R}} - k_{\boldsymbol{\omega}}\boldsymbol{e}_{\boldsymbol{\omega}} + \boldsymbol{\omega} \times \boldsymbol{J}\boldsymbol{\omega} - \boldsymbol{J}\left(\boldsymbol{\omega} \times \boldsymbol{R}^\top \boldsymbol{R}_d \boldsymbol{\omega}_d - \boldsymbol{R}^\top \boldsymbol{R}_d \dot{\boldsymbol{\omega}}_d\right). \end{aligned} \tag{11}$$

Operating directly on the nonlinear $\mathsf{SO}(3)$ manifold avoids the singularities present in minimal rotation parameterizations. This formulation provides almost-global asymptotic stability, meaning convergence to any desired pose from all initial conditions except a zero-measure set (*63*).

Disturbance compensation

The geometric controller guarantees exponential stability for the nominal dynamics in (1) and (4). In practice, MorphQuad encounters unknown disturbances such as wind and ground effects (*17, 19*). To maintain robust tracking, we augment the geometric controller with an $\mathcal{L}_1$ adaptive law

that estimates and cancels these disturbances in real time. The augmented dynamics are

$$\dot{\boldsymbol{p}} = \boldsymbol{v}, \qquad m\dot{\boldsymbol{v}} = m\boldsymbol{g} + \boldsymbol{R}\left(\boldsymbol{f}_{\text{Geo}} + \boldsymbol{f}_{\text{aug}}\right) + \boldsymbol{f}_d,$$
$$\dot{\boldsymbol{R}} = \boldsymbol{R}[\boldsymbol{\omega}]_\times, \quad \boldsymbol{J}\dot{\boldsymbol{\omega}} = -\boldsymbol{\omega} \times \boldsymbol{J}\boldsymbol{\omega} + \boldsymbol{\tau}_{\text{Geo}} + \boldsymbol{\tau}_{\text{aug}} + \boldsymbol{\tau}_d,$$

where $\boldsymbol{f}_{\text{aug}}$ and $\boldsymbol{\tau}_{\text{aug}}$ are the adaptive compensation terms in the body frame $\mathcal{B}$, and $\boldsymbol{f}_d$, $\boldsymbol{\tau}_d$ are the unknown disturbance force and torque. The adaptive force $\boldsymbol{f}_{\text{aug}}$ is expressed in $\mathcal{B}$ alongside the nominal force $\boldsymbol{f}_{\text{Geo}}$ and rotated to the world frame by $\boldsymbol{R}$, while the disturbance $\boldsymbol{f}_d$ acts in $\mathcal{W}$.

Defining the stacked velocity state $\boldsymbol{z} = [\boldsymbol{v}^\top \;\; \boldsymbol{\omega}^\top]^\top$, the dynamics can be written as

$$\dot{\boldsymbol{z}} = f(\boldsymbol{z}) + \boldsymbol{G}(\boldsymbol{R})\left(\boldsymbol{u}_{\text{Geo}} + \boldsymbol{u}_{\text{aug}}\right) + \boldsymbol{B}\,\boldsymbol{u}_d, \tag{12}$$

where

$$f(\boldsymbol{z}) = \begin{bmatrix} \boldsymbol{g} \\ -\boldsymbol{J}^{-1}\boldsymbol{\omega} \times \boldsymbol{J}\boldsymbol{\omega} \end{bmatrix}, \; \boldsymbol{G}(\boldsymbol{R}) = \begin{bmatrix} m^{-1}\boldsymbol{R} & \boldsymbol{0}_{3\times3} \\ \boldsymbol{0}_{3\times3} & \boldsymbol{J}^{-1} \end{bmatrix}, \; \boldsymbol{B} = \begin{bmatrix} m^{-1}\boldsymbol{I}_3 & \boldsymbol{0}_{3\times3} \\ \boldsymbol{0}_{3\times3} & \boldsymbol{J}^{-1} \end{bmatrix},$$
$$\boldsymbol{u}_{\text{Geo}} = [\boldsymbol{f}_{\text{Geo}}^\top \;\; \boldsymbol{\tau}_{\text{Geo}}^\top]^\top, \; \boldsymbol{u}_{\text{aug}} = [\boldsymbol{f}_{\text{aug}}^\top \;\; \boldsymbol{\tau}_{\text{aug}}^\top]^\top, \; \boldsymbol{u}_d = [\boldsymbol{f}_d^\top \;\; \boldsymbol{\tau}_d^\top]^\top.$$

The matrix $\boldsymbol{G}(\boldsymbol{R})$ maps body-frame control inputs to $\mathcal{W}$-frame accelerations via $\boldsymbol{R}$, while $\boldsymbol{B}$ maps the $\mathcal{W}$-frame disturbance force and the $\mathcal{B}$-frame disturbance torque.

The $\mathcal{L}_1$ adaptive controller consists of a state predictor, a piecewise-constant adaptation law, and a low-pass filter (LPF). At each control step, the algorithm uses the prediction error to estimate the disturbance and produces a filtered compensation signal.

The state predictor mirrors the plant dynamics with an additional error-injection term,

$$\dot{\hat{\boldsymbol{z}}} = f(\boldsymbol{z}) + \boldsymbol{G}(\boldsymbol{R})\left(\boldsymbol{u}_{\text{Geo}} + \boldsymbol{u}_{\text{aug}}\right) + \boldsymbol{h}(t) + \boldsymbol{A}_s\tilde{\boldsymbol{z}}, \tag{13}$$

where $\tilde{\boldsymbol{z}} = \hat{\boldsymbol{z}} - \boldsymbol{z}$ is the prediction error, $\boldsymbol{A}_s \in \mathbb{R}^{6\times6}$ is a user-selected diagonal Hurwitz matrix that governs the predictor convergence rate, and $\boldsymbol{h}(t) \in \mathbb{R}^6$ is the acceleration-space estimate of the total disturbance contribution $\boldsymbol{B}\,\boldsymbol{u}_d$ (*64*). The piecewise-constant adaptation law computes $\boldsymbol{h}$ and the corresponding disturbance estimate $\hat{\boldsymbol{u}}_d$ at each discrete time step k as

$$\boldsymbol{h}_k = -\left(\exp\left(\boldsymbol{A}_s T_s\right) - \boldsymbol{I}\right)^{-1} \boldsymbol{A}_s \exp\left(\boldsymbol{A}_s T_s\right) \tilde{\boldsymbol{z}}_k, \qquad \hat{\boldsymbol{u}}_{d,k} = -\boldsymbol{B}^{-1}\boldsymbol{h}_k, \tag{14}$$

where T_s is the sampling time. The force component of $\hat{\boldsymbol{u}}_{d,k}$ is rotated from $\mathcal{W}$ into $\mathcal{B}$ via $\boldsymbol{R}^\top$ before filtering. The estimate is then passed through first-order LPFs with separate bandwidths $\omega_{f,v}$ for force and $\omega_{f,\omega}$ for torque (both in rad/s), and the adaptive compensation $\boldsymbol{u}_{\mathrm{aug},k}$ is obtained by negating the filtered output.

Thrust allocation

As an overactuated omnidirectional platform, MorphQuad must convert the six-dimensional desired wrench $\boldsymbol{w} = [\boldsymbol{f}^\top \quad \boldsymbol{\tau}^\top]^\top$ into twelve low-level commands: four gimbal angle pairs (α_i, β_i) and four rotor speeds Ω_i. The allocation exploits the fact that each rotor's thrust direction and magnitude are independently controllable. Because the low-level commands α_i, β_i, and Ω_i of each rotor are decoupled, it suffices to find the four three-dimensional thrust vectors $\boldsymbol{t}_i$, from which the individual commands can be recovered.

We decompose each rotor's thrust vector, $\boldsymbol{t}_i$, into four additive terms: one quarter of the total desired force, plus three torque contributions for roll, pitch, and yaw. For a symmetric construction with half-length $l = |l_{i,x}|$, half-width $b = |l_{i,y}|$, and diagonal distance $r = \sqrt{l^2 + b^2}$ from the COM to each propeller, the per-rotor thrust vectors are

$$\begin{aligned}
\boldsymbol{t}_1 &= \frac{\boldsymbol{f}}{4} + \frac{\tau_x}{4b}\,\boldsymbol{k}_{\mathcal{B}} - \frac{\tau_y}{4l}\,\boldsymbol{k}_{\mathcal{B}} + \frac{\tau_z}{4r}\,\hat{\boldsymbol{e}}_{\psi_1}, \\
\boldsymbol{t}_2 &= \frac{\boldsymbol{f}}{4} - \frac{\tau_x}{4b}\,\boldsymbol{k}_{\mathcal{B}} - \frac{\tau_y}{4l}\,\boldsymbol{k}_{\mathcal{B}} + \frac{\tau_z}{4r}\,\hat{\boldsymbol{e}}_{\psi_2}, \\
\boldsymbol{t}_3 &= \frac{\boldsymbol{f}}{4} - \frac{\tau_x}{4b}\,\boldsymbol{k}_{\mathcal{B}} + \frac{\tau_y}{4l}\,\boldsymbol{k}_{\mathcal{B}} + \frac{\tau_z}{4r}\,\hat{\boldsymbol{e}}_{\psi_3}, \\
\boldsymbol{t}_4 &= \frac{\boldsymbol{f}}{4} + \frac{\tau_x}{4b}\,\boldsymbol{k}_{\mathcal{B}} + \frac{\tau_y}{4l}\,\boldsymbol{k}_{\mathcal{B}} + \frac{\tau_z}{4r}\,\hat{\boldsymbol{e}}_{\psi_4},
\end{aligned} \tag{15}$$

where $\boldsymbol{\tau} = [\tau_x \quad \tau_y \quad \tau_z]^\top$ are the scalar components of the desired torque. The unit vectors $\hat{\boldsymbol{e}}_{\psi_i}$ (denoting the yaw-torque direction for rotor i) lie in the $\boldsymbol{i}_{\mathcal{B}}$–$\boldsymbol{j}_{\mathcal{B}}$ plane, perpendicular to the corresponding rotor arms,

$$\hat{\boldsymbol{e}}_{\psi_1} = \begin{bmatrix} -b/r \\ l/r \\ 0 \end{bmatrix}, \quad \hat{\boldsymbol{e}}_{\psi_2} = \begin{bmatrix} b/r \\ l/r \\ 0 \end{bmatrix}, \quad \hat{\boldsymbol{e}}_{\psi_3} = \begin{bmatrix} b/r \\ -l/r \\ 0 \end{bmatrix}, \quad \hat{\boldsymbol{e}}_{\psi_4} = \begin{bmatrix} -b/r \\ -l/r \\ 0 \end{bmatrix}. \tag{16}$$

The decomposition in (15) is equivalent to the Moore-Penrose pseudo-inverse solution $\boldsymbol{t} = \boldsymbol{M}^{\dagger}\boldsymbol{w}$ with $\boldsymbol{M}^{\dagger} = \boldsymbol{M}^{\top}(\boldsymbol{M}\boldsymbol{M}^{\top})^{-1}$, which yields optimal thrust efficiency analogous to the minimum-norm allocation of a conventional quadrotor.

Since $\boldsymbol{t}_i = c_t \boldsymbol{G}_i(\alpha_i, \beta_i)\, \Omega_i^2$, the rotor speed and servo angles can be recovered from each thrust vector. Defining the unit thrust direction $\hat{\boldsymbol{t}}_i = \boldsymbol{t}_i / \|\boldsymbol{t}_i\|$ with components $\hat{\boldsymbol{t}}_i = [\hat{t}_{i,x} \;\; \hat{t}_{i,y} \;\; \hat{t}_{i,z}]^{\top}$, the trigonometric relations give

$$\Omega_i = \sqrt{\|\boldsymbol{t}_i\|/c_t}\,, \quad \text{and} \quad \begin{cases} \beta_i = \sin^{-1}(-\hat{t}_{i,y}), \quad \alpha_i = \operatorname{atan2}\big(\hat{t}_{i,x},\, \hat{t}_{i,z}\big)\,, \\ \beta_i = \pi - \sin^{-1}(\hat{t}_{i,y}), \quad \alpha_i = \pi + \operatorname{atan2}\big(\hat{t}_{i,x},\, \hat{t}_{i,z}\big)\,, \end{cases} \tag{17}$$

where $\operatorname{atan2}(\cdot,\cdot)$ is the two-argument arctangent. The two solution branches arise because $\sin(\cdot) = \sin(\pi - \cdot)$. The output of $\sin^{-1}(\cdot)$ lies in $[-\pi/2,\, \pi/2]$, so β_i can reach $[-\pi/2,\, 3\pi/2]$. Similarly, $\operatorname{atan2}(\cdot,\cdot)$ uses the signs of numerator and denominator to cover $[-\pi,\, \pi]$ for α_i. To minimize servo motion at each control step, we compare the current servo position $(\alpha_i',\, \beta_i')$ with all candidate solutions $\alpha_i + 2k\pi$ and $\beta_i + 2k\pi$ for $|k| \le n_r$, $k \in \mathbb{Z}$, and select the pair that minimizes $|\alpha_i' - \alpha_i - 2k\pi|$ and $|\beta_i' - \beta_i - 2k\pi|$ separately, where n_r constrains the maximum number of revolutions beyond one trigonometric period.

Enhancement for inter-rotor downwash and gimbal lock

We enhance the minimum-norm thrust allocation (15) to account for (a) inter-rotor downwash interference and (b) gimbal lock. In more detail: **(a) Inter-rotor aerodynamic interference.** When the desired torque $\boldsymbol{\tau} = \boldsymbol{0}$, the thrust allocation (15) yields co-linear thrust vectors $\boldsymbol{t}_i \parallel \boldsymbol{f}$ for all i. If the desired force is along $\boldsymbol{i}_{\mathcal{B}}$, the outer servo positions become $\alpha_i = \pm\pi/2$ with $\beta_i = 0$, so all four rotor systems point their downwash toward the opposing pair. This mutual interference invalidates the thrust model in (2) and reduces the effective thrust of the affected rotors. **(b) Gimbal lock.** If the desired force is along $\boldsymbol{j}_{\mathcal{B}}$ with $\boldsymbol{\tau} = \boldsymbol{0}$, the inner servo reaches $\beta_i = \pm\pi/2$, at which point $\cos\beta_i = 0$ and the outer servo α_i loses authority over the thrust direction. To illustrate the practical consequence, consider MorphQuad hovering at a $\pi/2$ roll angle so that $\boldsymbol{f} = [0 \;\; mg \;\; 0]^{\top}$. If the controller subsequently commands a small perturbation

$[\epsilon \;\; mg \;\; 0]^\top$ followed by $[-\epsilon \;\; mg \;\; 0]^\top$ at high frequency, the computed α_i would oscillate between $\pm\pi/2$, saturating the servos and destabilizing flight. This singularity shares the same mathematical root as mapping elements of $\mathbb{S}^2$ to $\mathbb{T}^2$.

We exploit the overactuation of MorphQuad to enable both enhancements through the null space of $\boldsymbol{M}$. Because $\boldsymbol{M} \in \mathbb{R}^{6\times 12}$ is a wide matrix, the linear system $\boldsymbol{w} = \boldsymbol{M}\boldsymbol{t}$ is underdetermined. The general solution takes the form

$$\boldsymbol{t} = \boldsymbol{M}^\dagger \boldsymbol{w} + \boldsymbol{N}_M \boldsymbol{c}, \tag{18}$$

where $\boldsymbol{N}_M$ is the null-space basis of $\boldsymbol{M}$ (constant rank six) and $\boldsymbol{c} \in \mathbb{R}^6$ is a coefficient vector that redistributes thrust among the rotors without changing the net wrench. The coefficients are chosen to satisfy two conditions: (i) adjacent rotor pairs must not have co-linear thrust vectors when $\boldsymbol{f} \parallel \boldsymbol{i}_\mathcal{B}$ or $\boldsymbol{f} \parallel \boldsymbol{j}_\mathcal{B}$, to prevent downwash interference, and (ii) no individual thrust vector may be parallel to $\boldsymbol{j}_\mathcal{B}$, to avoid gimbal lock.

To satisfy condition (ii) and the second part of condition (i), we set $c_1 = c_3 = c_5 = \langle \boldsymbol{f}/\|\boldsymbol{f}\|, \boldsymbol{j}_\mathcal{B}\rangle$. This introduces a component that repels each inner servo position away from $\beta_i = \pm\pi/2$, proportionally to how close the desired force direction is to the gimbal-lock axis. For the first part of condition (i), we tilt the rotor pair on top away from pointing directly at the bottom pair by setting

$$\begin{cases} c_2 = -c_4 = -\langle \boldsymbol{f}/\|\boldsymbol{f}\|, \boldsymbol{i}_\mathcal{B}\rangle, \;\; c_6 = 0, & \text{if } \langle \boldsymbol{f}/\|\boldsymbol{f}\|, \boldsymbol{i}_\mathcal{B}\rangle > 0, \\ c_2 = -c_4 = 0, \;\; c_6 = -\langle \boldsymbol{f}/\|\boldsymbol{f}\|, \boldsymbol{i}_\mathcal{B}\rangle, & \text{if } \langle \boldsymbol{f}/\|\boldsymbol{f}\|, \boldsymbol{i}_\mathcal{B}\rangle \le 0. \end{cases} \tag{19}$$

This conditional assignment ensures that the anti-parallel null-space perturbation is applied to whichever rotor pair axis is most aligned with the body-frame x-direction, breaking the co-linearity that would otherwise cause direct downwash impingement.

In summary, MorphQuad's control pipeline proceeds as follows: the geometric controller computes a desired six-dimensional wrench from $\mathsf{SE}(3)$ tracking errors, the $\mathcal{L}_1$ adaptation augments this wrench to reject disturbances, the thrust allocation decomposes the augmented wrench into individual rotor thrust vectors, and the null-space correction adjusts these vectors to avoid inter-rotor downwash interference and mechanical gimbal lock. The thrust vectors are then allocated to gimbal angles (α_i, β_i) and rotor speeds Ω_i through (17).

References

1. S. Park, J. Lee, J. Ahn, M. Kim, J. Her, G.-H. Yang, D. Lee, Odar: Aerial manipulation platform enabling omnidirectional wrench generation. *IEEE/ASME Transactions on mechatronics* **23** (4), 1907–1918 (2018).

2. D. Lee, B. Kim, H. J. Kim, Autonomous aerial manipulation at arbitrary pose in SE (3) with robust control and whole-body planning. *The International Journal of Robotics Research* p. 02783649251378195 (2025).

3. K. Bodie, M. Brunner, M. Pantic, S. Walser, P. Pfändler, U. Angst, R. Siegwart, J. Nieto, Active interaction force control for contact-based inspection with a fully actuated aerial vehicle. *IEEE Transactions on Robotics* **37** (3), 709–722 (2020).

4. M. Á. Trujillo, J. R. Martínez-de Dios, C. Martín, A. Viguria, A. Ollero, Novel aerial manipulator for accurate and robust industrial NDT contact inspection: A new tool for the oil and gas inspection industry. *Sensors* **19** (6), 1305 (2019).

5. S. Waharte, N. Trigoni, Supporting search and rescue operations with UAVs, in *2010 international conference on emerging security technologies* (IEEE) (2010), pp. 142–147.

6. W. Alawad, N. B. Halima, L. Aziz, An unmanned aerial vehicle (UAV) system for disaster and crisis management in smart cities. *Electronics* **12** (4), 1051 (2023).

7. D. Seneviratne, L. Ciani, M. Catelani, D. Galar, *et al.*, Smart maintenance and inspection of linear assets: An Industry 4.0 approach. *Acta Imeko* **7**, 50–56 (2018).

8. J. Anand, C. Aasish, S. S. Narayanan, R. A. Ahmed, Drones for disaster response and management, in *Internet of Drones* (CRC Press), pp. 177–200 (2023).

9. S. Xing, X. Zhang, J. Tian, C. Xie, Z. Chen, J. Sun, Morphing quadrotors: Enhancing versatility and adaptability in drone applications—A review. *Drones* **8** (12), 762 (2024).

10. M. Lyu, Y. Zhao, C. Huang, H. Huang, Unmanned Aerial Vehicles for Search and Rescue: A Survey. *Remote Sensing* **15** (13) (2023), doi:10.3390/rs15133266, https://www.mdpi.com/2072-4292/15/13/3266.

11. M. Zhao, F. Shi, T. Anzai, K. Chaudhary, X. Chen, K. Okada, M. Inaba, Flight motion of passing through small opening by dragon: Transformable multilinked aerial robot, in *2018 IEEE/RSJ International Conference on Intelligent Robots and Systems (IROS)* (IEEE) (2018), pp. 4735–4742.

12. F. Niroui, K. Zhang, Z. Kashino, G. Nejat, Deep Reinforcement Learning Robot for Search and Rescue Applications: Exploration in Unknown Cluttered Environments. *IEEE Robotics and Automation Letters* **4** (2), 610–617 (2019), doi:10.1109/LRA.2019.2891991.

13. M. Ruggia, C. Bermes, FLIFO: A Passively Morphing Drone for Small Gap Traversal, in *2025 International Conference on Unmanned Aircraft Systems (ICUAS)* (2025), pp. 214–221, doi:10.1109/ICUAS65942.2025.11007843.

14. P. Nooralishahi, C. Ibarra-Castanedo, S. Deane, F. López, S. Pant, M. Genest, N. P. Avdelidis, X. P. Maldague, Drone-based non-destructive inspection of industrial sites: A review and case studies. *Drones* **5** (4), 106 (2021).

15. A. Ollero, M. Tognon, A. Suarez, D. Lee, A. Franchi, Past, present, and future of aerial robotic manipulators. *IEEE Transactions on Robotics* **38** (1), 626–645 (2021).

16. H. Yang, S. Park, J. Lee, J. Ahn, D. Son, D. Lee, LASDRA: Large-Size Aerial Skeleton System with Distributed Rotor Actuation, in *2018 IEEE International Conference on Robotics and Automation (ICRA)* (2018), pp. 7017–7023, doi:10.1109/ICRA.2018.8460713.

17. Z. Xing, Y. Zhang, C.-Y. Su, Active Wind Rejection Control for a Quadrotor UAV Against Unknown Winds. *IEEE Transactions on Aerospace and Electronic Systems* **59** (6), 8956–8968 (2023), doi:10.1109/TAES.2023.3315254.

18. M. O'Connell, G. Shi, X. Shi, K. Azizzadenesheli, A. Anandkumar, Y. Yue, S.-J. Chung, Neural-fly enables rapid learning for agile flight in strong winds. *Science Robotics* **7** (66), eabm6597 (2022).

19. T. Yang, K. Chai, J. Ji, Y. Wu, C. Xu, F. Gao, Ground-Effect-Aware Modeling and Control for Multicopters. *IEEE/ASME Transactions on Mechatronics* **30** (6), 7406–7417 (2025), doi: 10.1109/TMECH.2025.3583162.

20. A. Garofano-Soldado, G. Heredia, A. Ollero, Aerodynamic interference in confined environments with tilted propellers: Wall effect and corner effect, in *2021 Aerial Robotic Systems Physically Interacting with the Environment (AIRPHARO)* (IEEE) (2021), pp. 1–8.

21. R. Watson, T. Zhao, D. Zhang, G. Dobie, C. MacLeod, S. G. Pierce, A fly-crawl-fly UAV for full-circumference inspection of non-magnetic pipes via thrust adhesion. *IEEE Transactions on Automation Science and Engineering* **22**, 24278–24293 (2025).

22. K. Alexis, G. Darivianakis, M. Burri, R. Siegwart, Aerial robotic contact-based inspection: planning and control. *Autonomous Robots* **40** (4), 631–655 (2016).

23. D. Brescianini, R. D'Andrea, Design, modeling and control of an omni-directional aerial vehicle, in *2016 IEEE international conference on robotics and automation (ICRA)* (IEEE) (2016), pp. 3261–3266.

24. S. Park, J. Her, J. Kim, D. Lee, Design, modeling and control of omni-directional aerial robot, in *2016 IEEE/RSJ International Conference on Intelligent Robots and Systems (IROS)* (IEEE) (2016), pp. 1570–1575.

25. M. Tognon, A. Franchi, Omnidirectional aerial vehicles with unidirectional thrusters: Theory, optimal design, and control. *IEEE Robotics and Automation Letters* **3** (3), 2277–2282 (2018).

26. M. Hamandi, K. Sawant, M. Tognon, A. Franchi, Omni-plus-seven (O7+): An omnidirectional aerial prototype with a minimal number of unidirectional thrusters, in *2020 International conference on unmanned aircraft systems (ICUAS)* (IEEE) (2020), pp. 754–761.

27. H. Lee, S. Cheng, Z. Wu, J. Lim, R. Siegwart, N. Hovakimyan, Geometric tracking control of omnidirectional multirotors for aggressive maneuvers. *IEEE Robotics and Automation Letters* **10** (2), 1130–1137 (2024).

28. R. Veenstra, A. Ali, C. Gabellieri, A. Franchi, 6D Physical Interaction with an Omnidirectional Aerial Robot. *Drones* **10** (2), 129 (2026).

29. M. Ryll, D. Bicego, M. Giurato, M. Lovera, A. Franchi, Fast-hex — a morphing hexarotor: design, mechanical implementation, control and experimental validation. *IEEE/ASME transactions on mechatronics* **27** (3), 1244–1255 (2021).

30. Y. Aboudorra, C. Gabellieri, R. Brantjes, Q. Sablé, A. Franchi, Modelling, analysis, and control of omnimorph: an omnidirectional morphing multi-rotor uav. *Journal of Intelligent & Robotic Systems* **110** (1), 21 (2024).

31. M. Ryll, H. H. Bülthoff, P. R. Giordano, Modeling and control of a quadrotor UAV with tilting propellers, in *2012 IEEE international conference on robotics and automation* (IEEE) (2012), pp. 4606–4613.

32. M. Ryll, H. H. Bülthoff, P. R. Giordano, A novel overactuated quadrotor unmanned aerial vehicle: Modeling, control, and experimental validation. *IEEE Transactions on Control Systems Technology* **23** (2), 540–556 (2014).

33. J. Li, J. Li, K. Kaneko, H. Liu, L. Shu, M. Zhao, Six-DoF Hand-Based Teleoperation for Omnidirectional Aerial Robots, in *2025 IEEE/RSJ International Conference on Intelligent Robots and Systems (IROS)* (IEEE) (2025), pp. 15482–15488.

34. M. Kamel, S. Verling, O. Elkhatib, C. Sprecher, P. Wulkop, Z. Taylor, R. Siegwart, I. Gilitschenski, The voliro omniorientational hexacopter: An agile and maneuverable tiltable-rotor aerial vehicle. *IEEE Robotics & Automation Magazine* **25** (4), 34–44 (2018).

35. R. Ji, J. Ma, S. S. Ge, Modeling and control of a tilting quadcopter. *IEEE Transactions on Aerospace and Electronic Systems* **56** (4), 2823–2834 (2019).

36. Skygauge Inspection, `https://www.skygauge.co/`, accessed: 2025-12-28.

37. Y. Luo, X. Cao, M. Lu, N. Chen, P. Lu, Agile Flight Through Tilted Spaces Using a Single-Servo Tilt-Rotor Quadrotor. *IEEE Transactions on Industrial Electronics* (2026).

38. Y. Su, P. Yu, M. J. Gerber, L. Ruan, T.-C. Tsao, Nullspace-based control allocation of overactuated UAV platforms. *IEEE robotics and automation letters* **6** (4), 8094–8101 (2021).

39. M. Zhao, K. Kawasaki, T. Anzai, X. Chen, S. Noda, F. Shi, K. Okada, M. Inaba, Transformable multirotor with two-dimensional multilinks: Modeling, control, and whole-body aerial manipulation. *The International Journal of Robotics Research* **37** (9), 1085–1112 (2018).

40. M. Zhao, K. Okada, M. Inaba, Versatile articulated aerial robot DRAGON: Aerial manipulation and grasping by vectorable thrust control. *The International Journal of Robotics Research* **42** (4-5), 214–248 (2023).

41. K. Bodie, Z. Taylor, M. Kamel, R. Siegwart, Towards efficient full pose omnidirectionality with overactuated mavs, in *International symposium on experimental robotics* (Springer) (2018), pp. 85–95.

42. K. Bodie, M. Brunner, M. Pantic, S. Walser, P. Pfndler, U. Angst, R. Siegwart, J. Nieto, An Omnidirectional Aerial Manipulation Platform for Contact-Based Inspection, in *Robotics: Science and Systems XV* (Robotics: Science and Systems Foundation) (2019), doi:10.15607/rss.2019.xv.019, `http://dx.doi.org/10.15607/RSS.2019.XV.019`.

43. H. Mayounove, C. Picaud, Omnidirectional Propelled Vehicle with Minimal Overall Dimensions (2023).

44. H. Mayounove, C. Picaud, G. Nicolas, Omnidirectional Vectored-Thrust Vehicle Comprising a Unit for Controlling the Orientation of Thrusters (2025).

45. I. Bao, J. C. D. P. G. Pacheco, A. Navsalkar, A. Scheffer, S. Shankar, A. Zhao, H. Zhou, V. Tzoumas, MorphEUS: Morphable OmnidirEctional Unmanned System, in *Proceedings of the IEEE International Conference on Robotics and Automation (ICRA), OCRAIM Workshop* (2025), `https://iral-morphable.github.io/`.

46. S. Bouabdallah, P. Murrieri, R. Siegwart, Design and control of an indoor micro quadrotor, in *IEEE International Conference on Robotics and Automation, 2004. Proceedings. ICRA'04. 2004* (IEEE), vol. 5 (2004), pp. 4393–4398.

47. D. Mellinger, N. Michael, V. Kumar, Trajectory generation and control for precise aggressive maneuvers with quadrotors. *The International Journal of Robotics Research* **31** (5), 664–674 (2012).

48. G. Michieletto, M. Ryll, A. Franchi, Fundamental actuation properties of multirotors: Force–moment decoupling and fail–safe robustness. *IEEE Transactions on Robotics* **34** (3), 702–715 (2018).

49. M. W. Mueller, R. D'Andrea, Stability and control of a quadrocopter despite the complete loss of one, two, or three propellers, in *2014 IEEE international conference on robotics and automation (ICRA)* (2014), pp. 45–52.

50. V. Artale, C. Milazzo, A. Ricciardello, Mathematical modeling of hexacopter. *Applied mathematical sciences* **7** (97), 4805–4811 (2013).

51. R. Rashad, J. Goerres, R. Aarts, J. B. C. Engelen, S. Stramigioli, Fully Actuated Multirotor UAVs: A Literature Review. *IEEE Robotics & Automation Magazine* **27** (3), 97–107 (2020), doi:10.1109/MRA.2019.2955964.

52. J. Xu, D. S. D'Antonio, D. Saldaña, H-modquad: Modular multi-rotors with 4, 5, and 6 controllable dof, in *2021 IEEE International Conference on Robotics and Automation (ICRA)* (IEEE) (2021), pp. 190–196.

53. D. Falanga, K. Kleber, S. Mintchev, D. Floreano, D. Scaramuzza, The foldable drone: A morphing quadrotor that can squeeze and fly. *IEEE Robotics and Automation Letters* **4** (2), 209–216 (2018).

54. S. Rajappa, M. Ryll, H. H. Bülthoff, A. Franchi, Modeling, control and design optimization for a fully-actuated hexarotor aerial vehicle with tilted propellers, in *2015 IEEE international conference on robotics and automation (ICRA)* (IEEE) (2015), pp. 4006–4013.

55. M. Ryll, D. Bicego, A. Franchi, Modeling and control of FAST-Hex: A fully-actuated by synchronized-tilting hexarotor, in *2016 IEEE/RSJ International Conference on Intelligent Robots and Systems (IROS)* (IEEE) (2016), pp. 1689–1694.

56. P. Zheng, X. Tan, B. B. Kocer, E. Yang, M. Kovac, TiltDrone: A fully-actuated tilting quadrotor platform. *IEEE Robotics and Automation Letters* **5** (4), 6845–6852 (2020).

57. S. H. Lee, Drone Having Multi-Degree-of-Freedom Flight Mode (2023).

58. X. Zhu, X. Zheng, K. Lu, H. Li, Omnidirectional Decoupled Circular Vector Tilt-Rotor Aircraft and Its Control Method (2024).

59. N. J. Seo, T. J. Armstrong, J. A. Ashton-Miller, D. B. Chaffin, Wrist strength is dependent on simultaneous power grip intensity. *Ergonomics* **51** (10), 1594–1605 (2008).

60. B. Nesbitt, *Handbook of valves and actuators: valves manual international* (Elsevier) (2011).

61. K. Huang, R. Rana, A. Spitzer, G. Shi, B. Boots, Datt: Deep adaptive trajectory tracking for quadrotor control. *arXiv preprint arXiv:2310.09053* (2023).

62. D. Mellinger, V. Kumar, Minimum snap trajectory generation and control for quadrotors, in *2011 IEEE international conference on robotics and automation* (IEEE) (2011), pp. 2520–2525.

63. T. Lee, M. Leok, N. H. McClamroch, Geometric tracking control of a quadrotor UAV on SE (3), in *49th IEEE conference on decision and control (CDC)* (IEEE) (2010), pp. 5420–5425.

64. Z. Wu, S. Cheng, P. Zhao, A. Gahlawat, K. A. Ackerman, A. Lakshmanan, C. Yang, J. Yu, N. Hovakimyan, L1Quad: L1 Adaptive Augmentation of Geometric Control for Agile Quadrotors With Performance Guarantees. *IEEE Transactions on Control Systems Technology* **33** (2), 597–612 (2025).

65. E. Sariyildiz, R. Oboe, K. Ohnishi, Disturbance observer-based robust control and its applications: 35th anniversary overview. *IEEE Transactions on Industrial Electronics* **67** (3), 2042–2053 (2019).

66. E. Tal, S. Karaman, Accurate tracking of aggressive quadrotor trajectories using incremental nonlinear dynamic inversion and differential flatness. *IEEE Transactions on Control Systems Technology* **29** (3), 1203–1218 (2020).

67. H. Zhou, V. Tzoumas, Simultaneous system identification and model predictive control with no dynamic regret. *IEEE Transactions on Robotics* (2025).

68. C. Zheng, W. Xu, Z. Zou, T. Hua, C. Yuan, D. He, B. Zhou, Z. Liu, J. Lin, F. Zhu, *et al.*, Fast-livo2: Fast, direct lidar–inertial–visual odometry. *IEEE Transactions on Robotics* **41**, 326–346 (2024).

69. Y. Ren, F. Zhu, G. Lu, Y. Cai, L. Yin, F. Kong, J. Lin, N. Chen, F. Zhang, Safety-assured high-speed navigation for mavs. *Science Robotics* **10** (98), eado6187 (2025).

70. J. Fishman, *Soft Aerial Manipulation*, Ph.D. thesis, Massachusetts Institute of Technology (2021).

71. J. Tucker, D. Liu, A. Swann, A. Ren, J. Yu, J. Sun, B. Kim, L. McGranahan, Q. Vuong, M. Schwager, π, But Make It Fly: Physics-Guided Transfer of VLA Models to Aerial Manipulation. *arXiv preprint arXiv:2603.25038* (2026).

72. G. Loianno, M. Watterson, V. Kumar, Visual inertial odometry for quadrotors on SE (3), in *2016 IEEE International Conference on Robotics and Automation (ICRA)* (IEEE) (2016), pp. 1544–1551.

73. Introduction to Intel® RealSense™ Visual SLAM and the T265 Tracking Camera, `https://dev.realsenseai.com/docs/intel-realsensetm-visual-slam-and-the-t265-tracking-camera`, accessed: 2026-03-27.

Acknowledgments

The authors thank the original team members Daniel Bernstein, Yanyu Chen, Laasya Chukka, and Monica Khalique, who contributed to the early development of the vehicle platform alongside A.Z. A video of the early prototype from 2022 is available at `https://www.youtube.com/watch?v=wFEDdiamtT8`. The project website, including supplementary videos and additional materials, is available at `https://iral-morphable.github.io/`.

Funding: This work was supported by the Michigan Translational Research and Commercialization (MTRAC) Advanced Transportation Innovation Hub, Mid-Stage Funding Program.

Author contributions: J.D.P.G.P. led the software development, including the control architecture, thrust allocation, firmware, and simulation, and conducted all experiments and data analysis. J.X. led the manuscript writing, visualization, and multimedia presentation, conducted all experiments, designed the thrust allocation strategy, and contributed to the controller design and augmen-

tation. A.Z. led the complete electromechanical design and fabrication of the novel quadrotor from system conception to implementation and flight, and supported the integration of the controller and firmware. H.Z. contributed to system design, visual-inertial odometry, controller design, and stability proof of the geometric controller. A.N. contributed to the original thrust allocation. A.S. and S.S. led initial firmware and simulation development. A.M.R. designed experimental end-effectors and assisted with vehicle assembly. Y.B. contributed to the early vehicle design. V.T. led the project. All authors reviewed and edited the manuscript.

Competing interests: The hardware design is the subject of pending U.S. patent application No. 63/703,312 (filed October 2024). The authors declare that they have no competing interests.

Supplementary Materials

Matrix Elements

$\boldsymbol{G}_i(\alpha_i, \beta_i)$ is the i-th column of $\boldsymbol{G}$, which is obtained by expanding the forward mapping from the rotor force to the body-frame force,

$$
\begin{aligned}
\boldsymbol{f} &= \sum_{i=1}^{4} \boldsymbol{R}_{\mathcal{P}_i}(\alpha_i, \beta_i) \left(c_t \Omega_i^2\right) \boldsymbol{k}_{\mathcal{P}_i} \\
&= \sum_{i=1}^{4} \boldsymbol{R}_j(\alpha_i) \boldsymbol{R}_i(\beta_i) \left(c_t \Omega_i^2\right) \boldsymbol{k}_{\mathcal{P}_i} \\
&= \sum_{i=1}^{4} \left(c_t \Omega_i^2\right) \begin{bmatrix} \cos\alpha_i & 0 & \sin\alpha_i \\ 0 & 1 & 0 \\ -\sin\alpha_i & 0 & \cos\alpha_i \end{bmatrix} \begin{bmatrix} 1 & 0 & 0 \\ 0 & \cos\beta_i & -\sin\beta_i \\ 0 & \sin\beta_i & \cos\beta_i \end{bmatrix} \begin{bmatrix} 0 \\ 0 \\ 1 \end{bmatrix} \\
&= c_t \begin{bmatrix} s\alpha_1 c\beta_1 & s\alpha_2 c\beta_2 & s\alpha_3 c\beta_3 & s\alpha_4 c\beta_4 \\ -s\beta_1 & -s\beta_2 & -s\beta_3 & -s\beta_4 \\ c\alpha_1 c\beta_1 & c\alpha_2 c\beta_2 & c\alpha_3 c\beta_3 & c\alpha_4 c\beta_4 \end{bmatrix} \begin{bmatrix} \Omega_1^2 \\ \Omega_2^2 \\ \Omega_3^2 \\ \Omega_4^2 \end{bmatrix}, \\
&= c_t \boldsymbol{G} \boldsymbol{\Omega}^{\circ 2}.
\end{aligned}
\tag{20}
$$

$$
\begin{aligned}
\boldsymbol{\tau} &= \sum_{i=1}^{4} \boldsymbol{l}_i \times \boldsymbol{t}_i, \\
&= \sum_{i=1}^{4} (c_t \Omega_i^2) \begin{bmatrix} l_{i,x} \\ l_{i,y} \\ l_{i,z} \end{bmatrix} \times \begin{bmatrix} c\alpha_i & s\alpha_i s\beta_i & s\alpha_i c\beta_i \\ 0 & c\beta_i & -s\beta_i \\ -s\alpha_i & c\alpha_i s\beta_i & c\alpha_i c\beta_i \end{bmatrix} \begin{bmatrix} 0 \\ 0 \\ 1 \end{bmatrix}, \\
&= \sum_{i=1}^{4} \left(c_t \Omega_i^2\right) \begin{bmatrix} l_{i,y} \cos\alpha_i \cos\beta_i + l_{i,z} \sin\beta_i \\ -l_{i,x} \cos\alpha_i \cos\beta_i + l_{i,z} \sin\alpha_i \cos\beta_i \\ -l_{i,x} \sin\beta_i - l_{i,y} \sin\alpha_i \cos\beta_i \end{bmatrix} \\
&= c_t \boldsymbol{H} \boldsymbol{\Omega}^{\circ 2},
\end{aligned}
\tag{21}
$$

where $\boldsymbol{H}^\top = \begin{bmatrix} l_{1,y}c\alpha_1 c\beta_1 + l_{1,z}s\beta_1 & -l_{1,x}c\alpha_1 c\beta_1 + l_{1,z}s\alpha_1 c\beta_1 & -l_{1,x}s\beta_1 - l_{1,y}s\alpha_1 c\beta_1 \\ l_{2,y}c\alpha_2 c\beta_2 + l_{2,z}s\beta_2 & -l_{2,x}c\alpha_2 c\beta_2 + l_{2,z}s\alpha_2 c\beta_2 & -l_{2,x}s\beta_2 - l_{2,y}s\alpha_2 c\beta_2 \\ l_{3,y}c\alpha_3 c\beta_3 + l_{3,z}s\beta_3 & -l_{3,x}c\alpha_3 c\beta_3 + l_{3,z}s\alpha_3 c\beta_3 & -l_{3,x}s\beta_3 - l_{3,y}s\alpha_3 c\beta_3 \\ l_{4,y}c\alpha_4 c\beta_4 + l_{4,z}s\beta_4 & -l_{4,x}c\alpha_4 c\beta_4 + l_{4,z}s\alpha_4 c\beta_4 & -l_{4,x}s\beta_4 - l_{4,y}s\alpha_4 c\beta_4 \end{bmatrix}$.

$$\boldsymbol{N}_M^\top = \begin{bmatrix} 0 & 0 & -1 & 0 & 0 & 1 & 0 & 0 & -1 & 0 & 0 & 1 \\ -\frac{l}{b} & -1 & 0 & \frac{l}{b} & 0 & 0 & 0 & 0 & 0 & 0 & 1 & 0 \\ -1 & 0 & 0 & 0 & 0 & 0 & 0 & 0 & 0 & 1 & 0 & 0 \\ -\frac{l}{b} & -1 & 0 & \frac{l}{b} & 0 & 0 & 0 & 1 & 0 & 0 & 0 & 0 \\ 0 & 0 & 0 & -1 & 0 & 0 & 1 & 0 & 0 & 0 & 0 & 0 \\ 0 & -1 & 0 & 0 & -1 & 0 & 0 & 0 & 0 & 0 & 0 & 0 \end{bmatrix}. \tag{22}$$

Proof of Reachability and Controllability

While this can be intuitively understood based on design, we formally prove that the system is controllable, with respect to force and torque produced. By this virtue, we claim in the theorem below that the system is reachable as well. This applies to all position and orientation states and their derivatives. To prove the reachability, we present a corollary which states that all forces and torques (within *reasonable* magnitude) can be achieved, proving the controllability argument.

Theorem 1 (Reachability)**.** *Given the drone dynamics* (1) *and* (4)*, force and torque relations* (8) *and sufficient limits on rotor velocities, all the states* $[\boldsymbol{p}^\top\ \boldsymbol{v}^\top\ \boldsymbol{R}^\top\ \boldsymbol{\omega}^\top]^\top$ *(position, linear velocity, rotation matrix, angular velocity) are reachable.*

Proof. By design, thrust vector by i^{th} rotor, $\boldsymbol{t}_i$ is given by

$$\boldsymbol{t}_i = c_t\Omega_i^2 \begin{bmatrix} \sin\alpha_i \cos\beta_i \\ -\sin\beta_i \\ \cos\alpha_i \cos\beta_i \end{bmatrix}, \tag{23}$$

where α_i and β_i are the servo motor angles, Ω_i is the angular velocity of i^{th} rotor and c_t is the thrust coefficient. Based on relation (23), we can always find a solution $(\alpha_i, \beta_i, \Omega_i)$ for any given $\boldsymbol{t}_i$, using sine and cosine inverses. In other words, any vector $\boldsymbol{t}_i$ can be achieved; hence, we consider the combined thrust vector $\boldsymbol{t} = [\boldsymbol{t}_1^\top\ \boldsymbol{t}_2^\top\ \boldsymbol{t}_3^\top\ \boldsymbol{t}_4^\top]^\top$, as a high-level control input.

Note: Only the magnitude of $\boldsymbol{t}_i$ has an upper limit, solely based on the maximum possible angular speed of propeller Ω_i. Any direction, based on servo angles α_i and β_i, can be commanded.

The forces and torques on the drone due to each of the propeller thrusts are given by

$$\begin{bmatrix} \boldsymbol{f} \\ \boldsymbol{\tau} \end{bmatrix} = \begin{bmatrix} \sum_{i=1}^{4} \boldsymbol{t}_i \\ \sum_{i=1}^{4} \boldsymbol{l}_i \times \boldsymbol{t}_i \end{bmatrix} = \begin{bmatrix} \boldsymbol{I} & \boldsymbol{I} & \boldsymbol{I} & \boldsymbol{I} \\ \boldsymbol{l}_1\times & \boldsymbol{l}_2\times & \boldsymbol{l}_3\times & \boldsymbol{l}_4\times \end{bmatrix} \begin{bmatrix} \boldsymbol{t}_1 \\ \boldsymbol{t}_2 \\ \boldsymbol{t}_3 \\ \boldsymbol{t}_4 \end{bmatrix} = \boldsymbol{M} \begin{bmatrix} \boldsymbol{t}_1 \\ \boldsymbol{t}_2 \\ \boldsymbol{t}_3 \\ \boldsymbol{t}_4 \end{bmatrix}, \tag{24}$$

where $\boldsymbol{M} = \begin{bmatrix} 1 & 0 & 0 & 1 & 0 & 0 & 1 & 0 & 0 & 1 & 0 & 0 \\ 0 & 1 & 0 & 0 & 1 & 0 & 0 & 1 & 0 & 0 & 1 & 0 \\ 0 & 0 & 1 & 0 & 0 & 1 & 0 & 0 & 1 & 0 & 0 & 1 \\ 0 & 0 & b & 0 & 0 & -b & 0 & 0 & -b & 0 & 0 & b \\ 0 & 0 & -l & 0 & 0 & -l & 0 & 0 & l & 0 & 0 & l \\ -b & l & 0 & b & l & 0 & b & -l & 0 & -b & -l & 0 \end{bmatrix}$, and l and b are the half-length and half-breadth of the drone, respectively, as shown in Equation (15). The linear mapping matrix $\boldsymbol{M} : \boldsymbol{t} \rightarrow (\boldsymbol{f}, \boldsymbol{\tau})$ is an underdetermined system since $\boldsymbol{M}$ is a 6×12 matrix with rank 6, which means that the columns of M span the vector space $\mathbb{R}^6$. Thus, this system of equations has infinite solutions. Since we always have a solution, we prove that any force/torque is achievable. Given the dynamics in eqs. (1) and (4), *i.e.*,

$$\dot{\boldsymbol{p}} = \boldsymbol{v}, \qquad m\dot{\boldsymbol{v}} = m\boldsymbol{g} + \boldsymbol{R}\boldsymbol{f},$$
$$\dot{\boldsymbol{R}} = \boldsymbol{R}[\boldsymbol{\omega}]_\times, \quad \boldsymbol{J}\dot{\boldsymbol{\omega}} = -\boldsymbol{\omega} \times \boldsymbol{J}\boldsymbol{\omega} + \boldsymbol{\tau},$$

and that the maximum limit on Ω_i is reasonable, so that the force/torque are always enough to counter gravity $\boldsymbol{g}$ and gyroscopic moments $-\boldsymbol{\omega} \times \boldsymbol{J}\boldsymbol{\omega}$, we prove that all states are *reachable*. □

Corollary 1 (Controllability)**.** *Since the solution for linear map $\boldsymbol{M}$ always exists, we can always find a set of thrust vectors $\boldsymbol{t}_i$, such that a desired force and torque is applied. Mathematically, given vectors $\boldsymbol{f}$ and $\boldsymbol{\tau}$, there exists $\boldsymbol{t} = [\boldsymbol{t}_1^\top \ \boldsymbol{t}_2^\top \ \boldsymbol{t}_3^\top \ \boldsymbol{t}_4^\top]^\top$, such that $\boldsymbol{f} = \sum_{i=1}^{4} \boldsymbol{t}_i, \boldsymbol{\tau} = \sum_{i=1}^{4} \boldsymbol{l}_i \times \boldsymbol{t}_i$. Hence, the system is controllable as all force and torque realizations are possible.*

Proof of Stability

Using the controller defined in (11), the corresponding closed loop error dynamics is

$$\dot{\boldsymbol{e}}_{\boldsymbol{p}} = \boldsymbol{e}_{\boldsymbol{v}} \tag{25}$$

$$\dot{\boldsymbol{e}}_{\boldsymbol{v}} = \frac{1}{m}\left(-k_{\boldsymbol{p}}\boldsymbol{e}_{\boldsymbol{p}} - k_{\boldsymbol{v}}\boldsymbol{e}_{\boldsymbol{v}}\right) \tag{26}$$

$$\dot{\boldsymbol{e}}_{\boldsymbol{R}} = \frac{1}{2}\left(tr\left(\boldsymbol{R}^{\top}\boldsymbol{R}_d\right)\boldsymbol{I} - \boldsymbol{R}^{\top}\boldsymbol{R}_d\right)\boldsymbol{e}_{\boldsymbol{\omega}} \tag{27}$$

$$\dot{\boldsymbol{e}}_{\boldsymbol{\omega}} = \boldsymbol{J}^{-1}\left(-k_{\boldsymbol{R}}\boldsymbol{e}_{\boldsymbol{R}} - k_{\boldsymbol{\omega}}\boldsymbol{e}_{\boldsymbol{\omega}}\right) \tag{28}$$

The error state $(\boldsymbol{e_p}, \boldsymbol{e_v}, \boldsymbol{e_R}, \boldsymbol{e_\omega}) = (\mathbf{0}, \mathbf{0}, \mathbf{0}, \mathbf{0})$ is an exponentially stable equilibrium of the closed loop dynamics. We define the regions of attraction in the following proposition.

Proposition 1 (Exponential Stability)**.** *Consider the controller defined in* (11)*. Suppose that the initial conditions satisfy*

$$\begin{aligned} \Psi\left(\boldsymbol{R}(0), \boldsymbol{R}_d(0)\right) &< 2, \\ \left\|\boldsymbol{e}_{\boldsymbol{\omega}}(0)\right\|^2 &< \frac{2k_{\boldsymbol{R}}}{\lambda_{\max}(\boldsymbol{J})}\left(2 - \Psi\left(\boldsymbol{R}(0), \boldsymbol{R}_d(0)\right)\right), \end{aligned} \tag{29}$$

where a real-valued error function $\Psi(\cdot,\cdot) : \mathsf{SO}(3) \times \mathsf{SO}(3) \to \mathbb{R}$ *is defined as* $\Psi\left(\boldsymbol{R}, \boldsymbol{R}_d\right) \triangleq \frac{1}{2}\operatorname{tr}\left(I - \boldsymbol{R}_d^{\top}\boldsymbol{R}\right)$*. Then, the zero equilibrium of the closed-loop tracking error* $(\boldsymbol{e_p}, \boldsymbol{e_v}, \boldsymbol{e_R}, \boldsymbol{e_\omega}) = (\mathbf{0}, \mathbf{0}, \mathbf{0}, \mathbf{0})$ *is exponentially stable.*

We define the Lyapunov Candidate for the attitude dynamics. Let a Lyapunov candidate $\mathcal{V}_2$ be

$$\mathcal{V}_2 = \frac{1}{2}\boldsymbol{e}_{\boldsymbol{\omega}}^{\top}\boldsymbol{J}\boldsymbol{e}_{\boldsymbol{\omega}} + k_{\boldsymbol{R}}\Psi\left(\boldsymbol{R}, \boldsymbol{R}_d\right) + c_2\boldsymbol{e}_{\boldsymbol{R}}^{\top}\boldsymbol{e}_{\boldsymbol{\omega}}, \tag{30}$$

where c_2 is a non-negative constant. Suppose the initial condition in eq. (29) is satisfied, it follows directly (*63, Proposition 1*) that

$$z_2^{\top} M_{21} z_2 \leq \mathcal{V}_2 \leq z_2^{\top} M_{22} z_2 \tag{31}$$

$$\dot{\mathcal{V}}_2 \leq -z_2^{\top} W_2 z_2 \tag{32}$$

where $z_2 = \begin{bmatrix} \|\boldsymbol{e_R}\| \\ \|\boldsymbol{e_\omega}\| \end{bmatrix}$, $M_{21} = \frac{1}{2}\begin{bmatrix} k_{\boldsymbol{R}} & -c_2 \\ -c_2 & \lambda_{\min}(\boldsymbol{J}) \end{bmatrix}$, $M_{22} = \frac{1}{2}\begin{bmatrix} \frac{2k_{\boldsymbol{R}}}{2-\psi_2} & c_2 \\ c_2 & \lambda_{\max}(\boldsymbol{J}) \end{bmatrix}$, $\psi_2 = \frac{1}{k_R}\mathcal{V}_2|_{t=0,c_2=0}$, and $W_2 = \begin{bmatrix} \frac{c_2 k_{\boldsymbol{R}}}{\lambda_{\max}(\boldsymbol{J})} & -\frac{c_2 k_{\boldsymbol{\omega}}}{2\lambda_{\min}(\boldsymbol{J})} \\ -\frac{c_2 k_{\boldsymbol{\omega}}}{2\lambda_{\min}(\boldsymbol{J})} & k_{\boldsymbol{\omega}} - c_2 \end{bmatrix}$.

The matrices W_2, M_{21}, and M_{22} are positive-definite by choosing c_2 such that

$$c_2 < \min\left\{k_{\boldsymbol{\omega}}, \frac{4k_{\boldsymbol{\omega}}k_{\boldsymbol{R}}\lambda_{\min}(J)^2}{k_{\omega}^2\lambda_{\max}(\boldsymbol{J}) + 4k_{\boldsymbol{R}}\lambda_{\min}(\boldsymbol{J})^2}, \sqrt{k_{\boldsymbol{R}}\lambda_{\min}(\boldsymbol{J})}\right\} \tag{33}$$

For translation dynamics, let a Lyapunov candidate $\mathcal{V}_1$ be

$$\mathcal{V}_1 = \frac{1}{2}k_{\boldsymbol{p}}\|\boldsymbol{e_p}\|^2 + \frac{1}{2}m\|\boldsymbol{e_v}\|^2 + c_1\boldsymbol{e_p}^\top\boldsymbol{e_v} \tag{34}$$

where c_1 is a positive constant. Clearly, we have

$$z_1^\top M_{11} z_1 \leq \mathcal{V}_1 \leq z_1^\top M_{12} z_1 \tag{35}$$

where $z_1 = \begin{bmatrix} \|\boldsymbol{e_p}\| \\ \|\boldsymbol{e_v}\| \end{bmatrix}$, $M_{11} = \frac{1}{2}\begin{bmatrix} k_{\boldsymbol{p}} & -c_1 \\ -c_1 & m \end{bmatrix}$, and $M_{12} = \frac{1}{2}\begin{bmatrix} k_{\boldsymbol{p}} & c_1 \\ c_1 & m \end{bmatrix}$.

The derivative of $\mathcal{V}_1$ is given by

$$\begin{aligned}
\dot{\mathcal{V}}_1 =& k_{\boldsymbol{p}}\boldsymbol{e_p}^\top\boldsymbol{e_v} + \boldsymbol{e_v}^\top\left(-k_{\boldsymbol{p}}\boldsymbol{e_p} - k_{\boldsymbol{v}}\boldsymbol{e_v}\right) + c_1\boldsymbol{e_v}^\top\boldsymbol{e_v} + \frac{c_1}{m}\boldsymbol{e_p}^\top\left(-k_{\boldsymbol{p}}\boldsymbol{e_p} - k_{\boldsymbol{v}}\boldsymbol{e_v}\right) \\
=& -\left(k_{\boldsymbol{v}} - c_1\right)\|\boldsymbol{e_v}\|^2 - \frac{c_1 k_{\boldsymbol{p}}}{m}\|\boldsymbol{e_p}\|^2 - \frac{c_1 k_{\boldsymbol{v}}}{m}\boldsymbol{e_p}^\top\boldsymbol{e_v} \\
\leq& -z_1^\top W_1 z_1
\end{aligned} \tag{36}$$

where $W_1 = \begin{bmatrix} k_{\boldsymbol{v}} - c_1 & -\frac{c_1 k_{\boldsymbol{v}}}{2m} \\ -\frac{c_1 k_{\boldsymbol{v}}}{2m} & \frac{c_1 k_{\boldsymbol{p}}}{m} \end{bmatrix}$. The matrices W_1, M_{11}, and M_{12} are positive-definite by choosing a positive constant c_1 such that

$$c_1 < \min\left\{\frac{4mk_{\boldsymbol{p}}k_{\boldsymbol{v}}}{4k_{\boldsymbol{p}} + k_{\boldsymbol{v}}^2}, \sqrt{mk_{\boldsymbol{p}}}\right\}. \tag{37}$$

Now let $\mathcal{V} = \mathcal{V}_1 + \mathcal{V}_2$ be the Lyapunov candidate of the complete system,

$$\mathcal{V} = \frac{1}{2}k_{\boldsymbol{p}}\|\boldsymbol{e_p}\|^2 + \frac{1}{2}m\|\boldsymbol{e_v}\|^2 + c_1\boldsymbol{e_p}^\top\boldsymbol{e_v} + \frac{1}{2}\boldsymbol{e_\omega}^\top\boldsymbol{J}\boldsymbol{e_\omega} + \boldsymbol{k_R}\Psi\left(\boldsymbol{R}, \boldsymbol{R}_d\right) + c_2\boldsymbol{e_R}^\top\boldsymbol{e_\omega} \tag{38}$$

The bound of the Lyapunov candidate $\mathcal{V}$ can be written as

$$z_1^T M_{11} z_1 + z_2^T M_{21} z_2 \leq \mathcal{V} \leq z_1^T M_{12} z_1 + z_2^T M_{22} z_2. \tag{39}$$

The time derivative of $\mathcal{V}$ is given by

$$\dot{\mathcal{V}} \leq -z_1^T W_1 z_1 - z_2^T W_2 z_2. \tag{40}$$

By choosing c_1 and c_2 such that eqs. (33) and (37) are satisfied, we obtain that $\mathcal{V}$ is positive definite, and $\dot{\mathcal{V}}$ is negative definite. Therefore, we conclude that the zero equilibrium of the tracking errors of the complete dynamics is exponentially stable. □

We obtain exponential stability of the generalized geometric controller for almost every pair of $(\boldsymbol{R}(0), \boldsymbol{R}_d(0))$. Specifically, Proposition 1 holds for $\Psi(\boldsymbol{R}(0), \boldsymbol{R}_d(0)) < 2$, which indicates the initial attitude error between $\boldsymbol{R}(0)$ and $\boldsymbol{R}_d(0)$ should be less than $180°$. In other words, we prove that the closed-loop controller is exponentially stable in *almost* the entire $\mathsf{SO}(3)$. This result improves the exponential stability of the geometric controller of a regular quadrotor, which requires the initial attitude error between $\boldsymbol{R}(0)$ and $\boldsymbol{R}_d(0)$ to be less than $90°$ (*63*).

Proof of Thrust Distribution Optimality

Theorem 2 (Optimality)**.** *The Thrust Distribution given by* (15) *is the optimal solution with respect to the cost function*

$$E(\boldsymbol{t}) = \frac{1}{2}\sum_{i=1}^{4} ||\boldsymbol{t}_i||_2^2. \tag{41}$$

Proof. The constraints for the problem are given by $\boldsymbol{f} = \sum_{i=1}^{4} \boldsymbol{t}_i$ and $\boldsymbol{\tau} = \sum_{i=1}^{4} \boldsymbol{l}_i \times \boldsymbol{t}_i$. The Lagrangian for the constrained optimization problem is given by

$$\mathcal{L}(\boldsymbol{t}) = \frac{1}{2}\sum_{i=1}^{4} ||t_i||_2^2 + \lambda^\intercal \left(\boldsymbol{f} - \sum_{i=1}^{4} \boldsymbol{t}_i\right) + \mu^\intercal \left(\boldsymbol{\tau} - \sum_{i=1}^{4} \boldsymbol{l}_i \times \boldsymbol{t}_i\right). \tag{42}$$

The gradient of Lagrangian is $\nabla\mathcal{L} = \left[\left(\frac{\partial\mathcal{L}}{\partial \boldsymbol{t}_1}\right)^\top \quad \left(\frac{\partial\mathcal{L}}{\partial \boldsymbol{t}_2}\right)^\top \quad \left(\frac{\partial\mathcal{L}}{\partial \boldsymbol{t}_3}\right)^\top \quad \left(\frac{\partial\mathcal{L}}{\partial \boldsymbol{t}_4}\right)^\top\right]^\top$. Without loss of generality, we expand $\frac{\partial\mathcal{L}}{\partial \boldsymbol{t}_1}$ using appropriate values for $\boldsymbol{r}_i$, and equating it with 0, we get

$$\frac{\partial\mathcal{L}}{\partial \boldsymbol{t}_1} = \begin{bmatrix} \partial\mathcal{L}/\partial t_{1x} \\ \partial\mathcal{L}/\partial t_{1y} \\ \partial\mathcal{L}/\partial t_{1z} \end{bmatrix} = \begin{bmatrix} t_{1x} - \lambda_1 - \mu_3(-b) \\ t_{1y} - \lambda_2 - \mu_3(l) \\ t_{1z} - \lambda_3 - (\mu_1 b - \mu_2 l), \end{bmatrix} = 0.$$

Equivalently, we have

$$\boldsymbol{t}_1 = \lambda + \begin{bmatrix} 0 & 0 & -b \\ 0 & 0 & l \\ b & -l & 0 \end{bmatrix} \mu.$$

Similarly, solving further for all $\frac{\partial \mathcal{L}}{\partial \boldsymbol{t}_2} = 0$, $\frac{\partial \mathcal{L}}{\partial \boldsymbol{t}_3} = 0$, $\frac{\partial \mathcal{L}}{\partial \boldsymbol{t}_4} = 0$, and constraints $\boldsymbol{f} = \sum_{i=1}^{4} \boldsymbol{t}_i$ and $\boldsymbol{\tau} = \sum_{i=1}^{4} \boldsymbol{l}_i \times \boldsymbol{t}_i$, the solution for multipliers λ and μ is

$$\lambda = \frac{\boldsymbol{f}}{4}, \qquad \mu = \begin{bmatrix} \tau_x/4b^2 \\ \tau_y/4l^2 \\ \tau_z/4r^2 \end{bmatrix}. \tag{43}$$

Substituting these in the solutions for $\boldsymbol{t}_i$, we get

$$\boldsymbol{t}_1 = \boldsymbol{f}/4 + \begin{bmatrix} 0 & 0 & -b/r^2 \\ 0 & 0 & l/r^2 \\ 1/b & -1/l & 0 \end{bmatrix} \boldsymbol{\tau}/4, \qquad \boldsymbol{t}_2 = \boldsymbol{f}/4 + \begin{bmatrix} 0 & 0 & b/r^2 \\ 0 & 0 & l/r^2 \\ -1/b & -1/l & 0 \end{bmatrix} \boldsymbol{\tau}/4$$

$$\boldsymbol{t}_3 = \boldsymbol{f}/4 + \begin{bmatrix} 0 & 0 & b/r^2 \\ 0 & 0 & -l/r^2 \\ -1/b & 1/l & 0 \end{bmatrix} \boldsymbol{\tau}/4, \qquad \boldsymbol{t}_4 = \boldsymbol{f}/4 + \begin{bmatrix} 0 & 0 & -b/r^2 \\ 0 & 0 & -l/r^2 \\ 1/b & 1/l & 0 \end{bmatrix} \boldsymbol{\tau}/4.$$

This is the same as the solutions proposed in the inverse mapping equations (15).

Equivalently, we can use the linear map $\boldsymbol{M} : \boldsymbol{t} \to (\boldsymbol{f}, \boldsymbol{\tau})$ to find the solution. Since we already proved that this is an underdetermined system with infinite solutions, we can use pseudo-inverse $\boldsymbol{M}^\dagger = \boldsymbol{M}^\top \left(\boldsymbol{M}\boldsymbol{M}^\top\right)^{-1}$ to find the suitable $\boldsymbol{t}_i$ values, *i.e.*,

$$\boldsymbol{t} = \boldsymbol{M}^\dagger \begin{bmatrix} \boldsymbol{f}^\top & \boldsymbol{\tau}^\top \end{bmatrix}^\top. \tag{44}$$

The pseudo-inverse gives a minimum norm-squared solution among the infinite solutions, *i.e.,* $\min \frac{1}{2}||\boldsymbol{t}||_2^2$, which is same as cost function, $E(\boldsymbol{t})$. The further expansion of the expression (44) gives the same solution as the proposed inverse mapping. □